NTNU – Trondheim
Norwegian University of
Science and Technology

Beam - Column Connections Subjected to Static and Dynamic Loading

Herman Frich

MASTER THESIS 2014

SUBJECT AREA:	DATE:	NO. OF PAGES:
Computational Mechanics	11 June 2014	57 + 18

TITLE:

Beam – Column Connections Subjected to Static and Dynamic Loading

Bjelke-søyle – forbindelser påkjent av statisk og dynamisk last

BY:

Herman Frich

SUMMARY:

In recent years, an increased awareness has been on the reliability of bolted connections in extreme events, such as the loss of a load bearing column in a terrorist attack. The ability to transfer the forces through the joints is key to maintain the structural integrity and prevent a progressive collapse of buildings. Sudden dynamic loading may cause a shift in the response behavior that is not captured by common design methods, which are often based on static conditions.

This thesis investigates the behaviour of a bolted steel connection in a column removal scenario. Experimental tests have been conducted under rapid, non-cyclic loading conditions and simplified methods based on European design standards (Eurocode) as well as advanced numerical analyses have been compared to the experimental results. The goal was to reveal possible implications on design of joints to improve the safety of structures.

The experimental tests showed that the assembly failed in flexure, typical for moment connections. This was true for both quasi-static and dynamic loading conditions, and was predicted by the simplified design method and the numerical models. However, the numerical simulations revealed that rapid loading caused a transition from the typical bending- to shear action due to inertia effects.

NORGES TEKNISK-NATURVITENSKAPELIGE UNIVERSITET
INSTITUTT FOR KONSTRUKSJONSTEKNIKK

MASTER THESIS 2014

Herman Frich

Beam – Column Connections Subjected to Static and Dynamic Loading

(Bjelke-søyle – forbindelser påkjent av statisk og dynamisk last)

It is important to understand the behaviour of connections subjected to extreme loads, *e.g.* dropped objects and sudden column-removal scenarios. Connections are often the critical component in a structure, and if they fail, progressive collapse is imminent. Bolted steel connections are common in various structures such as office buildings and off-shore platforms. There are established design rules for these connections, *e.g.* Eurocode NS-EN 1993-1-8. However, these design rules are based on various assumptions and simplifications. An important one is that quasi-static conditions are assumed. It is therefore interesting to investigate the behaviour of these connections through experiments and numerical analyses and compare them with the Eurocode.

In this master thesis, a double-sided beam – column connection will be tested and analysed. The beams have an endplate welded onto one of the ends. The endplates are bolted to the column flanges. The research project has three main objectives: (1) determine the material properties of the various components of the connection, (2) investigate experimentally the behaviour of the bolted steel connection, and (3) compare the experimental results with analyses from the finite element method and Eurocode.

Some keywords for activities related to this master thesis project may include:
- Literature survey: Behaviour of bolted connections (articles, codes, text books).
- Material tests: Uniaxial tension tests. Identification of parameters for numerical model.
- Component tests: Quasi-static and possibly dynamic tests on a bolted end-plate connection. The connection will be tested with a direction of the load such that tension will occur in the lower beam flanges.
- Numerical analyses: FEM simulations of component tests. Validation of model.
- Design code: The capacity and the stiffness of the connection determined from experiments and numerical analyses should be compared with estimates from Eurocode NS-EN 1993-1-8.

The candidate may agree with the supervisors to pay particular attention to specific parts of the investigation, or include other aspects than those already mentioned.

The thesis is to be organized as a research report, recognizing the guidelines provided by Department of Structural Engineering.

Supervisors: Erik Grimsmo, Arne Aalberg and Arild Holm Clausen

The report is to be handed in not later than 11 June 2014.

NTNU, 13 January 2014

Arild Holm Clausen

Preface

This thesis is finalized at the end of the spring semester of 2014 and concludes my Master of Science degree at NTNU. The work has been a part of an experimental program carried out at the Structural Impact Laboratory (SIMLab).

Over the past years I have developed an interest in the practical application of the finite element method in structural analysis problems. Therefore, I would like to thank professor Arild Holm Clausen for introducing me to the subject of Computational Methods in Structural Mechanics. His encouraging approach to teaching has been much appreciated.

Gratitude is also extended to my supervisor, PhD candidate Erik Løhre Grimsmo, whose guidance and support have helped me a lot in writing this thesis, the results would not have been the same.

Finally, I would like to honor my fellow students, Gjermund Båsen and Torger Nordgård, for valuable discussions throughout this semester.

<center>
Trondheim, June 2014

Herman Frich
</center>

Abstract

Bolted beam-column connections are commonly used in office buildings and off-shore platforms in Norway. The use of pre-fabricated components in frame structures is popular due to the cost effective and quick erection of buildings, where engineered members can be manufactured with great accuracy in a controlled environment at a fabrication shop.

In recent years, an increased awareness has been on the reliability of these connections in extreme events, such as the loss of a load bearing column in a terrorist attack. A lack of study on bolted connections under dynamic loading has been revealed, and a number of experimental programs have been initiated.

The ability to transfer the forces through the joints is key to maintain the structural integrity and prevent a progressive collapse in buildings. In addition, sudden dynamic loading may cause a shift in the response behavior that is not captured by common design methods, which are often based on static conditions.

Therefore, a test program was initiated to investigate the behavior of a bolted connection under rapid, non-cyclic loading in a column removal scenario. Experimental tests of a beam-column assembly were conducted under quasi-static and dynamic loading conditions.

Simplified calculations based on European design standards (Eurocode) as well as advanced numerical analyses were performed and compared directly to the experimental findings. The goal was to reveal possible implications on design of joints to extreme loads to improve the safety of structures.

The experimental tests revealed that the assembly failed in flexure, typical for moment connections. This was true for both quasi-static and dynamic loading conditions, and was predicted by the simplified design method and the numerical models. However, an overly safe estimate of the capacity was obtained by Eurocode's design method.

Furthermore, the numerical simulations revealed that rapid loading caused a transition from the typical bending- to shear action due to inertia effects. Further investigation into what type of load regime that will cause a change from flexural to shear failure has therefore been proposed for further work.

Sammendrag

Skrudde bjelke-søyleforbindelser er mye brukt i næringsbygg og oljeplattformer i Norge. Prefabrikkerte komponenter i rammekonstruksjoner er populært på grunn av en kostnadseffektiv og rask oppføring av nybygg fordi stålkomponentene kan produseres i et kontrollert miljø på et mekanisk verksted.

Det har i de senere årene vært en økende oppmerksomhet på påliteligheten til disse forbindelsene i ekstreme lasttilfeller, for eksempel ved tap av en bærende søyle i et terrorangrep. Relativt få studier har blitt gjort på skrudde forbindelser utsatt for dynamiske laster, og har ført til at en rekke eksperimentelle testprogrammer har blitt iverksatt.

Evnen til å overføre krefter gjennom knutepunktene er avgjørende for å opprettholde bæreevnen og hindre en progressiv kollaps ved tap av søyler i bygninger. I tillegg kan en plutselig dynamisk belastning forårsake endringer i responsen som ikke fanges opp av vanlige beregningsmetoder, som ofte er basert på statiske forhold.

Et testprogram ble derfor startet opp for å undersøke oppførselen til en skrueforbindelse under plutselig, ikke-syklisk belastning. Fullskala tester av en bjelke-søyle forbindelse ble gjennomført under kvasistatiske og dynamiske belastningsforhold.

Forenklede beregninger basert på europeiske standarder (Eurocode) samt avanserte numeriske analyser ble utført og sammenlignet med de eksperimentelle resultatene. Målet var å avdekke mulige mangler i disse beregningsmodellene og dermed øke sikkerheten til bygninger.

De eksperimentelle testene viste at forbindelsen gikk til brudd i bøyning, typisk for momentstive forbindelser. Dette gjaldt for både kvasistatiske og dynamiske belastningsforhold, og ble forutsagt av den forenklede beregningsmodellen og de numeriske beregningene. Imidlertid ga metoden presentert i standarden et for konservativt estimat av kapasiteten.

Resultatene viste også at en rask belastning forårsaket endringer i lastfordelingen. Skjærkreftenes relative påvirkning økte på grunn av treghetskrefter i de dynamiske simuleringene. Derfor ble det foreslått å gå videre med å undersøke hvilke dynamiske lastforhold som vil føre til skjærbrudd.

Contents

VIII

List of symbols

ΔL Change in gauge length of tensile specimen

Δ Vertical displacement of column

δ Opening of end-plate relative to column flange

$\dot{p}$ Plastic strain rate

μ Coefficient of friction

ν Poisson's ratio

ϕ Joint rotation

ρ Mass density

σ_0 Initial yield stress

σ_{avg} Average stress in tensile specimen $\left(\frac{F}{A}\right)$

σ_{eq} Equivalent stress

σ_{ij} Stress component

σ_i Principal stress component

ε_f Fracture strain

ε_{ij} Strain component

ε_i Principal strain component

ζ Triaxial stress correction function

A Cross section of tensile specimen

c Viscous stress exponent, see Eq. (6)

E Elastic modulus

e Engineering strain

F Axial force in tensile specimen

f Yield function

f_u Ultimate tensile strength

f_y Yield strength

$F_{t,Rd}$ Tension resistance of bolt

I_b Area moment of inertia of the beam cross section

k_i Linear spring stiffness

$k_{\phi,ini}$ Initial rotational stiffness of joint

k_ϕ Rotational stiffness of joint

k_{eq} Equivalent stiffness

L Gauge length of tensile specimen

L_b Length of beam, see Figure 13

L_c Beam span used in design, see Figure 13

L_ϕ Length of connection, see Figure 13

L_s Beam span used in experimental tests, see Figure 26

M_{Ed} Design moment

$M_{j,Rd}$ Moment resistance of joint

P Vertical column force

p Plastic strain

p_u Plastic strain at maximum load in tensile specimen

p_{eq} Equivalent plastic strain

R Isotropic hardening

s Engineering stress

t Thickness of tensile specimen

V_{Ed} Design shear force

w Width of tensile specimen

W_c Internal strain energy at fracture

z Lever arm

1   Introduction

1.1   Bolted connections subjected to extreme loads

Bolted steel connections are commonly used in office buildings and off-shore platforms in Norway, usually to ensure the vertical load bearing of floors. Standardized sections and plates can be welded together with great accuracy in a fabrication shop using specialized machinery. The manufactured assemblies allows for a quick erection of a complete frame structure at the construction site, therefore reducing the uncertainties regarding the costs.

The structural integrity is usually achieved in the design process through simplified models of the structural system, where each component must resist the applied loads in an ultimate limit state [1]. Abnormal loads are included in the accidental limit state design.

A column removal scenario
An example of an undesired incident that may be included in an accidental limit state is depicted in Figure 1. An explosive blast or collision has lead to the removal of a central column in a frame structure.
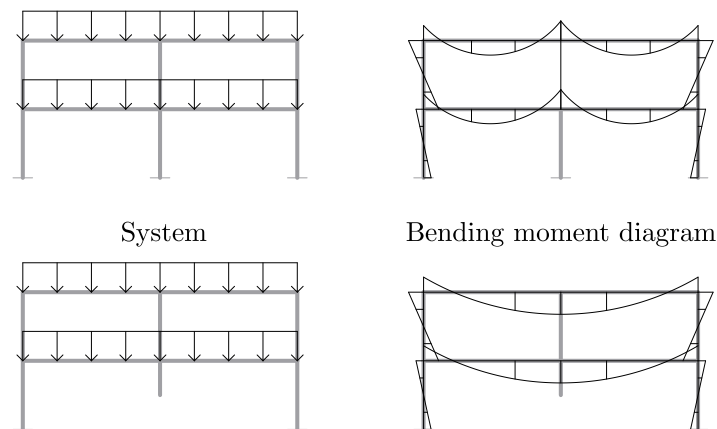

Figure 1: *Frame structure under a design load case (top) and under a column removal scenario (bottom).*

Loss of vertical load bearing causes a sudden transfer of forces, and the bending moment diagram reveals that the loading direction is reversed. Thus, joints that are optimized to transfer the design forces may function poorly.

Furthermore, structural components such as hollow core slabs can loose support and fall onto subjacent floors. If a column is hit suddenly, the acceleration of the surrounding beams will generate inertia forces that acts in the opposite direction as illustrated in Figure 2. The inertial resistance will have a positive effect on the bending moment at midspan, but the shear forces will have a relatively higher impact. Shear failure may therefore be of great importance when loads are applied suddenly.
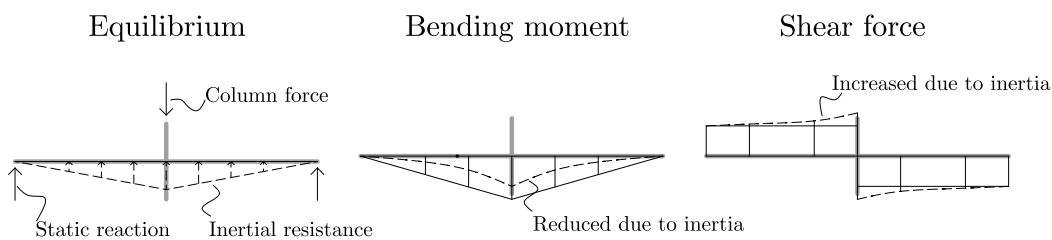

Figure 2: *Dynamic equilibrium in a central column removal scenario.*

1.2 Previous work

An extensive test program of bolted end-plate connections under static loading was undertaken by Coelho et al. [2]. One of the objectives was to evaluate the design methods proposed by Eurocode [3], which is used to determine the capacity and stiffness of joints. They found that increasing the thickness of the end-plate in a beam-column connection will generally increase resistance, but decrease ductility and hence the rotational capacity of the joint. Eurocode gave safe estimates for joint resistance and rotational capacity, but overestimated the initial stiffness. They proposed that new procedures must be developed for estimation of rotational capacity, which was overly conservative according to the standard.

Experimental tests and numerical simulations of various moment connections under a central column removal scenario have been conducted by Yang and Tan [4, 5] and Sadek et al. [6, 7]. The focus has been on studying the effects of *catenary action*. An initial flexural behavior and a gradual plastification typical for moment connections were observed. However, the assemblies failed under a combination of bending- and axial stress. An increase in the vertical load capacity by as much as 100 % was observed for flush end-plate connections due to catenary action [5]. A sufficiently ductile behavior was essential, and many welded connections did not

show a significant increase in capacity. Response characteristics and failure modes were accurately captured by non-linear finite element models [4, 7].

While a great deal of studies have been carried out on steel moment-connections subjected to cyclic loading, relatively few publications have been on moment connections subjected to short impulse loading. Most of these focus on blast loading of frame structures, not the individual joints. However, numerical studies such as the one carried out by Subawala et al. [8] revealed that the finite element method can be used to assess the stress distribution in moment connections under blast loading.

In despite of efforts, no research studies of bolted beam-column connections subjected to short impulse loads have been found.

1.3 Experimental program

This thesis is part of an ongoing experimental test program carried out at the Structural Impact Laboratory (SIMLab) to study the behavior of a bolted end-plate connection under rapid, non-cyclic loading. The double-sided connection consists of two beam members with welded end-plates bolted to a column as depicted in Figure 3. The beams (HEA180), column (HEB220) and plates are of standard structural grade steel S355, while the bolts (M16) are of class 8.8.
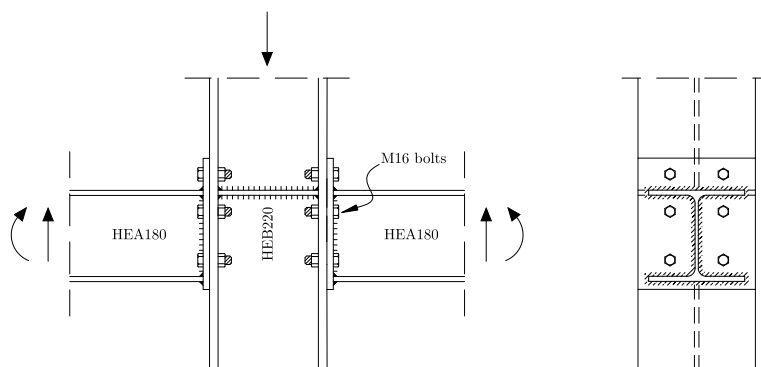

Figure 3: *Double sided connection investigated in the experimental test program.*

The joint is designed to fail in flexure due to large tensile forces in the top flange, which is the typical load case in a frame structure as illustrated in Figure 1. The joint is therefore optimized to transfer the design moment by having an extended end-plate in the upper part. The performance of the joint in this particular design configuration was investigated in a parallel Master's thesis by Baasen and Nordgaard [9].

3

1.4   Scope of thesis

In the extreme event of a sudden loss of vertical support, the load direction is reversed as illustrated by the arrows in Figure 3. This is the basis of the experimental tests studied in this thesis. In addition, ordinary design methods as well as advanced numerical analyses have been performed and compared to the experimental results. The simplified methods used in design codes rely on various assumptions to allow for hand calculations. An important one is static conditions, therefore neglecting any dynamic effects. Non-linear finite element analysis can be a powerful tool when used properly, and is indispensable when the response is to be determined until failure. However, it is essential to be aware of the limitations in these numerical models.

Objective
The thesis objective is twofold: (1) investigate how typical design methods manage to predict failure when load direction is reversed and (2) reveal if sudden dynamic loading will significantly change the characteristics in response and failure mode, in particular shear failure of bolts or welds.

Outline
The thesis is divided into 8 sections as shown below:

- Section 2, Theory: most of the underlying theory used in this thesis is presented.

- Section 3, Design of joint to Eurocode 3: the capacity and stiffness are determined according to methods proposed by Eurocode.

- Section 4, Material tests: the material test program is presented. The focus is on how important material properties were extracted from the test data.

- Section 5, Experimental tests of joints: the experimental test program is explained and important results are given.

- Section 6, Finite element simulations: the numerical model used to simulate the experimental tests is established and tested for sensitivities.

- Section 7, Discussion: the simplified design method as well as the finite element predictions are compared to the experimental results. The changes in the response characteristics due to sudden dynamic loading have been emphasized.

- Section 8, Conclusions and suggestions for further work: the main findings are given and possible improvements are proposed for future studies.

2 Theory

Simple hand calculations and non-linear finite element simulations are used to predict the response of the connection in Figure 3. A summary of the most important underlying theory used throughout the thesis is presented in the subsequent sections.

First, in Section 2.1, the principle of virtual work applied to yield line design is given. This is the basis of the Component method in Eurocode 3.

The constitutive model of a rate dependent elasto-plastic material used in the finite element model is presented in Section 2.2.

Finally, in Section 2.3-2.4, the development of a finite stress-strain measure is given. The focus is on how an elasto-plastic material model can be calibrated from tensile tests.

2.1 Yield line design

Yield line design is a method used to find the ultimate load capacity of transversely loaded plates. The theory is a generalization of the plastic hinge method used for beams in frame structures, and can be found in the book by Larsen [10].

Basic principle
All deformations are localized along specific *yield lines*, which forms a failure mechanism. All other parts remain elastic and move as rigid bodies. It follows from the principle of virtual work that the work done by rotation along the plastic yield lines (W_P) must be equal to the work done by the externally applied load (W_E):

$$W_P = W_E \tag{1}$$

It can be shown that the work done by rotation around the yield line is the same as the work done by rotation along the projected length of the yield line onto the support axis (see Figure 4), and a simple expression for the internal plastic work can be found:

$$W_P = \Sigma m_P \cdot \phi_i \cdot l_i \tag{2}$$

where $m_P = f_y \cdot t^2/4$ is the moment resistance per unit length of a plate with thickness t and a yield stress of f_y. Furthermore, l_i is the length of the projected yield line onto the support axis with angle ϕ_i.

The external work is taken as the force multiplied with displacement:

$$W_E = \int q(x,y) \cdot w(x,y) \cdot dA \tag{3}$$

where $q(x, y)$ is the applied load per unit area and $w(x, y)$ is the transverse displacement.

The critical load is obtained by finding the mechanism which requires the least amount of work to develop. Therefore, an infinite number of different mechanisms must be checked.

Simple problem
An example is presented to illustrate how the method can be used in design. A simply supported plate with sides a is loaded by a point load P and the capacity is determined for the yield line mechanism shown in Figure 4.
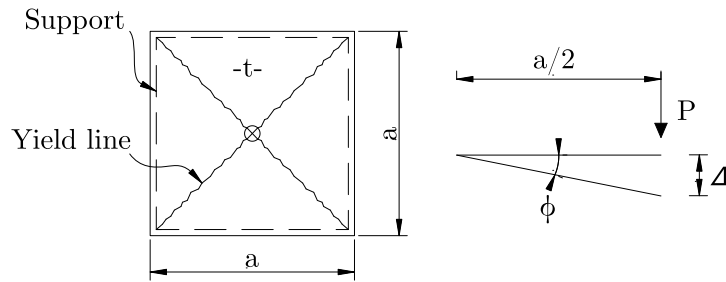
Figure 4: *Simply supported plate subjected to point load.*

The projected yield line length is $\Sigma l_i = 4a$ with a rotation angle $\phi = 2\Delta/a$. The internal work is calculated from Eq. (2):

$$W_p = m_p \cdot 4a \cdot \frac{2\Delta}{a} = 8 \cdot m_p \cdot \Delta$$

The external work is obtained from Eq. (3) by multiplying the load with the vertical displacement:

$$W_E = P \cdot \Delta$$

Demanding energy conservation (Eq. (1)) and solving for the applied load gives the limit state capacity:

$$P = 8 \cdot m_p$$

Yield line design applied to beam-column connections

Due to complex geometries and loading conditions in real life structures, the critical failure mechanism can be difficult to find. One example is bending of a column flange in a bolted beam-column connection as shown in Figure 5.
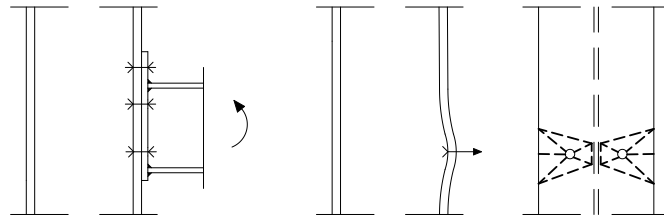

Figure 5: Possible yield mechanism for a column flange in bending.

Simplified T-stub models have therefore been developed and implemented in design codes. These are based on the underlying principle of yield line design and validated by experimental tests. A limited number of failure mechanisms must be checked as shown in Figure 6. The ultimate capacity will depend on the thickness of plates, the placement of bolts and the material strength.
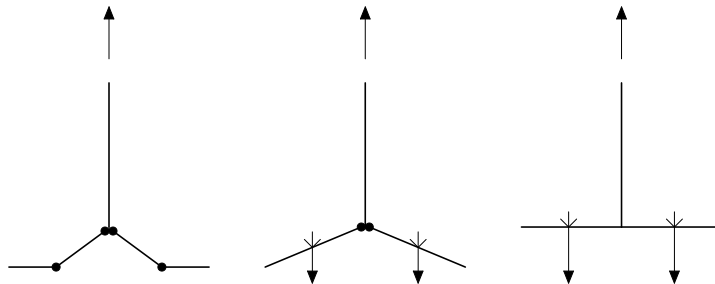
Figure 6: Failure mechanisms for T-stub model used in Eurocode [3]. Yielding of plate (left), bolt failure and yielding of plate (middle) and bolt failure (right)

2.2 Constitutive model

An outline of the theory behind a rate-dependent plasticity model with isotropic work hardening will be given. The presented theory is based on lectures given by Hopperstad and Boervik [11], and can be found in books by Irgens [12], Lubliner [13] and Lemaitre and Chaboche [14].
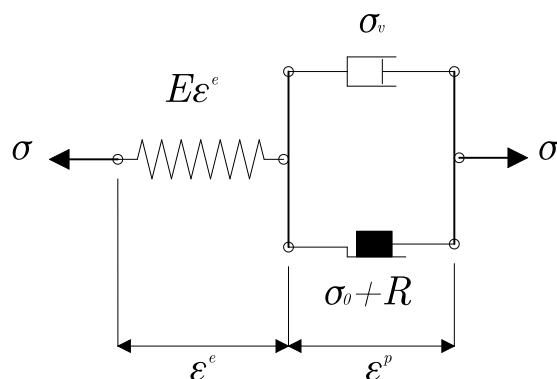

Figure 7: *Rheological illustration of constitutive model.*

The basic principles of the constitutive model are illustrated for a uniaxial stress state in Figure 7. There is an elastic spring corresponding to the reversible deformation, coupled in series with a dashpot and a friction element, which allows for plastic dissipation and irreversible deformation.

Elasticity

Under small deformations, metals will generally show a linear stress-strain relationship. Hooke's law for isotropic material in three spatial dimensions is given as:

$$
\begin{bmatrix} \sigma_{11} \\ \sigma_{22} \\ \sigma_{33} \\ \sigma_{12} \\ \sigma_{23} \\ \sigma_{13} \end{bmatrix} = \frac{E}{(1+\nu)(1-2\nu)} \begin{bmatrix} (1-\nu) & \nu & \nu & 0 & 0 & 0 \\ \nu & (1-\nu) & \nu & 0 & 0 & 0 \\ \nu & \nu & (1-\nu) & 0 & 0 & 0 \\ 0 & 0 & 0 & (1-2\nu)/2 & 0 & 0 \\ 0 & 0 & 0 & 0 & (1-2\nu)/2 & 0 \\ 0 & 0 & 0 & 0 & 0 & (1-2\nu)/2 \end{bmatrix} \begin{bmatrix} \varepsilon_{11} \\ \varepsilon_{22} \\ \varepsilon_{33} \\ 2\varepsilon_{12} \\ 2\varepsilon_{23} \\ 2\varepsilon_{13} \end{bmatrix}
$$

Yielding

Yielding is initiated when the material is stressed beyond its yield limit, and atoms begin to slide relative to each other. Mathematically, the yield criterion (f) can be expressed as:

$$ f = \sigma_{eq} - \sigma_0 = 0 $$

where σ_{eq} is the equivalent stress (scalar) and σ_0 is the initial yield stress of the material.

The von Mises yield stress is most commonly used for isotropic materials and can be written as:

$$\sigma_{eq} = \sqrt{\frac{(\sigma_1 - \sigma_2)^2 + (\sigma_2 - \sigma_3)^2 + (\sigma_1 - \sigma_3)^2}{2}}$$

where σ_i is the principal stress components. In the case of uniaxial stress ($\sigma_2 = \sigma_3 = 0$), the Mises stress will be reduced to:

$$\sigma_{eq} = \sigma_1 \tag{4}$$

Plastic flow

A material undergoes irreversible plastic deformations during yielding. The von Mises yield criterion together with an associated flow rule gives:

$$\dot{\varepsilon}_{ij}^p = \frac{3\sigma_{ij}'}{2\sigma_{eq}}\dot{p}_{eq}$$

where σ_{ij}' denotes the deviatoric stress and the equivalent plastic strain (p_{eq}) is taken as an accumulated plastic flow:

$$\dot{p}_{eq} = \sqrt{\frac{3}{2}\dot{\varepsilon}_{ij}^p\dot{\varepsilon}_{ij}^p}$$

$$p_{eq} = \int_0^t \dot{p}_{eq}dt$$

Work hardening

Additional strength due to movement of dislocations in material is often observed, and the yield stress will increase when material exhibits plastic flow. Isotropic hardening is suitable for problems involving large plastic deformation without abrupt change in load direction, where the Bauschinger effect become important.

The yield criterion can therefore be taken as:

$$f = \sigma_0 + R(p_{eq}) \tag{5}$$

where R is the strain hardening function.

Viscous stress

Ductile metals show an increase in yield strength and flow stress when rate of straining increases. Strain rate dependency is often included on a multiplicative form:

$$\sigma_{eq} = (\sigma_0 + R)(1 + \frac{\dot{p}}{\dot{p}_0})^c \tag{6}$$

where c is the parameter which determines the rate sensitivity and $\dot{p}_0$ is a reference strain rate. Observe that the equivalent stress simply scales with viscous term in Eq. (6) and do not depend on the plastic strain.

Fracture

A ductile fracture criterion proposed by Cockcroft and Latham [15] is adopted in this thesis. Fracture occur when the strain energy per unit volume reaches a critical value:

$$W_c = \int_0^{\varepsilon_f} max(\sigma_1, 0)d\varepsilon_1 \tag{7}$$

where the subscript 1 denotes the maximum principal direction and ε_f is the fracture strain. Observe that only tensile stress is contributing to fracture, hence tensile separation is the underlying concept.

2.3 Uniaxial tension test

The uniaxial tension test is a widely used mechanical test to determine material properties such as strength and ductility. This section gives an outline of the theory going from force and geometry measurements of a specimen to a true stress-strain relationship used as input in finite element codes.

True strain and stress relations

Force (F), displacement (ΔL), width (w) and thickness (t) are continuously measured during a uniaxial tensile test.
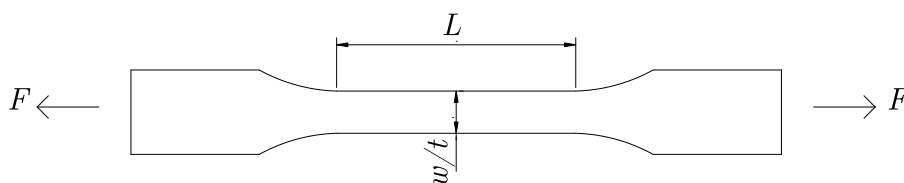

Figure 8: *Typical coupon used in a uniaxial tension test.*

Engineering stress-strain measures are calculated based on the undeformed geometry as shown in Eq. (8a) and Eq. (8b) simply by dividing the elongation by the initial length and force by the initial cross sectional area.

$$e = \frac{\Delta L}{L_0} \tag{8a}$$

$$s = \frac{F}{A_0} \tag{8b}$$

Their validity is restricted to small strains, and will not produce accurate results in a tensile test where both specimen length and cross sectional area are severely altered. Thus, if large strains are expected, new measures are needed.

A common approach is to introduce a *logarithmic stress-strain relationship* given in Eq. (9a) and Eq. (9b), which can be established by integrating the strain:

$$d\varepsilon = \frac{dL}{L} \Rightarrow \int_0^\varepsilon d\varepsilon = \int_{L_0}^L \frac{dL}{L} \Rightarrow \varepsilon = \ln L - \ln L_0 = \ln \frac{L}{L_0}$$

and by assuming plastic incompressibility (volume preservation):

$$\frac{A}{A_0} = \frac{L_0}{L}$$

which leads to:

$$\varepsilon = \ln \frac{L}{L_0} = \ln(1 + e) \tag{9a}$$

$$\sigma = \frac{F}{A} = \frac{F}{A_0}\frac{L}{L_0} = s(1 + e) \tag{9b}$$

The logarithmic stress-strain relationship can also be expressed solely by the cross sectional area:

$$\varepsilon = \ln \frac{L}{L_0} = \ln \frac{A_0}{A} \tag{10a}$$

$$\sigma = \frac{F}{A} \tag{10b}$$

Stress triaxiality

Necking is a geometric instability that occur when the increase in strength due to strain hardening is less than the increase in stress due to the reduction in cross sectional area. Strain localization in the necked region of the specimen introduces a multi-axial state of stress as depicted in Figure 9, and the relationship given in Eq. (4) is therefore not valid.
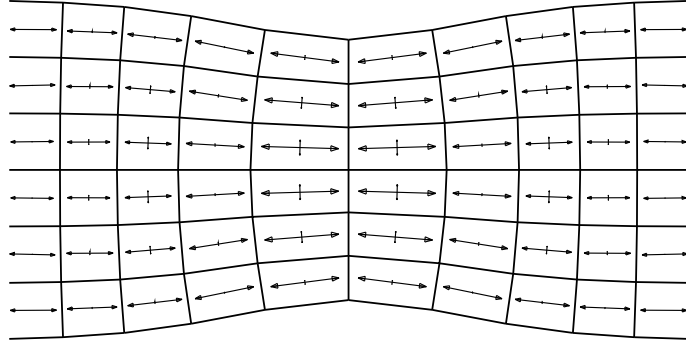
Figure 9: *Principal stress components in neck region.*

An estimate of the equivalent stress - plastic strain relationship can be obtained by multiplying the average stress in the longitudinal direction ($\sigma_{avg} = \frac{F}{A}$) with a *triaxial stress correction function* (ζ):

$$\sigma_{eq} = \zeta \sigma_{avg} \tag{11}$$

$$\zeta \begin{cases} = 1 & p_{eq} < p_u \\ < 1 & p_{eq} > p_u \end{cases}$$

where p_u is the plastic strain at time of neck initiation (maximum load). Therefore, the triaxial stress correction is only active during necking.

Empirical relations have been found for a variety of width-to-thickness ratios and materials for rectangular cross sections. However, a study by Yazzie et al. [16] revealed that a general neck correction has not been found for rectangular specimens.

By utilizing axis symmetry and by making basic assumptions about the neck geometry, Bridgman [17] found an analytical solution for circular specimens:

$$\zeta_{Bridgman} = \frac{1}{(1 + 2R/a)\ln(1 + a/2R)}$$

where a is the cross sectional radius and R is the radius of the neck contour, assumed to be circular.

2.4 Digital image correlation (DIC)

Various optical instrument techniques have been developed to capture rigid body motion and local strains during mechanical tests. One such method, *digital image*

correlation, has been increasing in popularity over the past decades due to easy setup and use [18]. The basic principles explained in this section are based on planar deformations, but the theory can be extended to three dimensional analyses.

Concept

A series of high resolution bit-map images are captured with a camera pointing perpendicular to a flat surface. Each pixel is represented as a gray-scale value in a matrix making up the picture. Two such matrices F and G of the undeformed (x, y) and deformed $(x*, y*)$ configuration are shown in Figure 10.
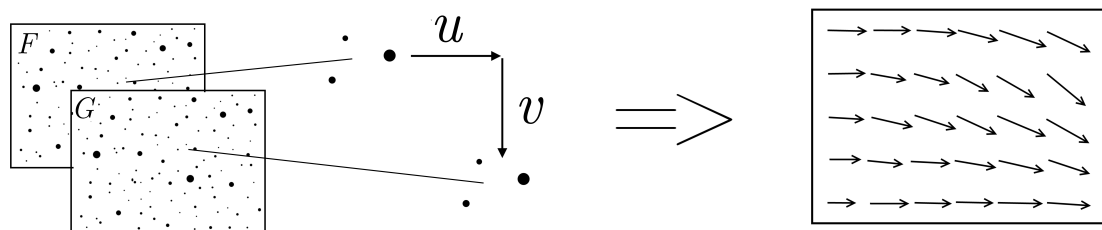
Figure 10: *Conceptual representation of a DIC analysis. Bitmap images (left) and displacement field (right).*

The cross correlation coefficient (r_{ij}) describes how the two matrices are related around a specific pixel. If perfectly correlated, the coefficient will have the maximum value of 1.

$$r_{ij} = 1 - \frac{\Sigma_i \Sigma_j [F(x_i, y_j) - \bar{F}][G(x*_i, y*_j) - \bar{G}]}{\sqrt{\Sigma_i \Sigma_j [F(x_i, y_j) - \bar{F}]^2 \Sigma_i \Sigma_j [G(x*_i, y*_j) - \bar{G}]^2}}$$

A change in position can be described by linear deformation theory with displacements u and v:

$$x* = x + u + \frac{du}{dx}\Delta x + \frac{du}{dy}\Delta y$$

$$y* = y + v + \frac{dv}{dy}\Delta y + \frac{dv}{dx}\Delta x$$

Varius search routines have been proposed to find displacements (u,v) which maximizes the correlation function (r). By discretization of the displacement field into subset of pixels and by using Newton-Raphson iterations Sutton et al. [19] managed to create search algorithms which were at least 20-times faster than available in 1986.

3   Design of joint to Eurocode 3

The bolted beam-column joint studied in the experimental test program (Figure 3) has been analyzed using methods established by Eurocode. Moment capacity and rotational stiffness are calculated according to the *Component method* in NS-EN-1993-1-8 [3]. See Appendix A and B for complete calculations.

3.1   Capacity

The connection depicted in Figure 11 is idealized by a set of components, which are designed to transfer the external forces. Each component is checked for sufficient capacity for forces acting at the periphery of the column web panel. To allow for hand calculations, an equivalent T-stub model is used in Eurocode as described in Section 2.1. Material- and load coefficients are set to 1.0, and material parameters such as yield stress (f_y) and ultimate tensile strength (f_u) are obtained from tensile tests.
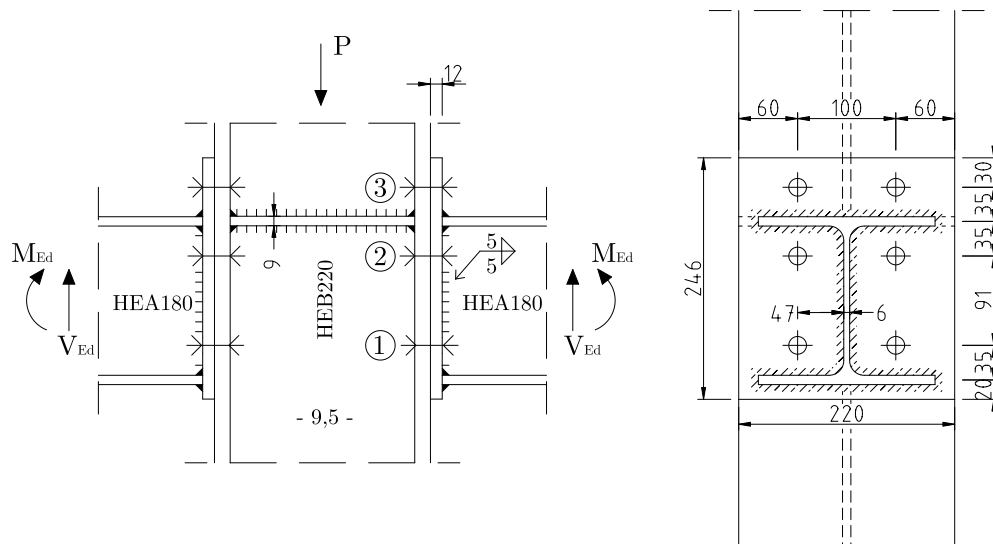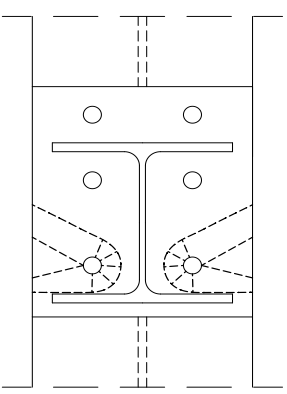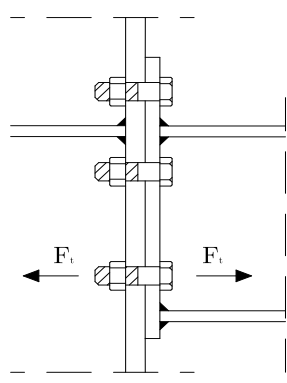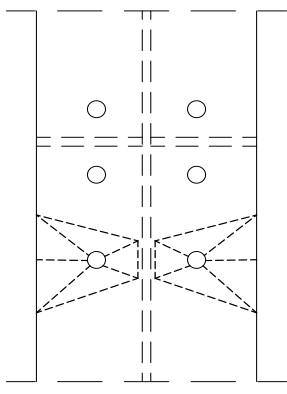

Figure 11: Joint geometry.

The center of compression is set to the top flange, while bolt row ① is the only row considered active in tension. Tensile forces in bolt row ② are neglected because of a relatively small lever arm. Compressive flange force and tension forces in row ① are therefore carrying the external moment M_{Ed}. Bolt row ③ is designed to carry the shear force V_{Ed}.

14

Yielding of the end-plate and bolt failure in row ① is calculated to be the critical failure mechanism with moment resistance $M_{j,Rd} = 31.2$ kNm. A description of the three most critical failure mechanisms found are given in Table 1. The shear capacity V_{Rd} is found to be 182 kN.

Table 1: *Critical failure mechanisms found by the Component method*

	Failure mechanism	Utilization
	Bolt failure and yielding of end-plate. Non-circular pattern with an effective T-stub length of 310 mm.	1.00
	Bolt failure. Ultimate tensile capacity reached for bolts in row ①.	0.92
	Bolt failure and yielding of column flange. Non-circular pattern with an effective T-stub length of 198 mm.	0.82

3.2 Stiffness

Rotational stiffness

A simplified stiffness model has been created as shown in Figure 12, where the structural components are represented as linear springs coupled in series.
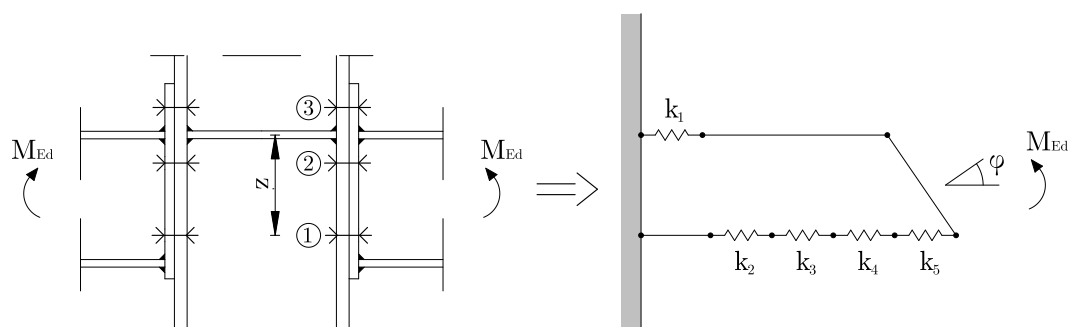

Figure 12: *Stiffness model used in the Component method.*

The stiffness contribution from each component is based on elastic deformation of specific zones in the connection. Simple equations have been established in Eurocode, where the elastic modulus, cross sectional area and geometry determines the stiffness value. The results are listed in Table 2.

Table 2: *Stiffness of components*

Spring	Component	Stiffness [$k \cdot 10^{-6}$ N/mm]
k_1	Stiffened column web in compression	∞
k_2	Column web in tension	1.78
k_3	Column flange in bending	5.11
k_4	End-plate in bending	1.20
k_5	Bolt row ① in tension	1.35

Some calculations are needed to establish a moment-rotation relationship. The following equations are derived from Eurocode. Note that a different notation has been used.

The equivalent stiffness (k_{eq}) for the tensile springs coupled in series is found by:

$$k_{eq} = \frac{1}{\frac{1}{k_2} + \frac{1}{k_3} + \frac{1}{k_4} + \frac{1}{k_5}}$$

The *initial rotational stiffness* ($k_{\phi,ini}$) can be established by considering the lever arm (z) in Figure 12:

$$k_{\phi,ini} = k_{eq}z^2$$

To account for a reduction in stiffness due to plasticity, the initial stiffness is decreased gradually until the moment capacity is reached:

$$k_\phi = \begin{cases} k_{\phi,ini} & M_{Ed} \leq \frac{2}{3}M_{j,Rd} \\ \\ k_{\phi,ini}(1.5\frac{M_{Ed}}{M_{j,Rd}})^{-2.7} & \frac{2}{3}M_{j,Rd} < M_{Ed} \leq M_{j,Rd} \end{cases}$$

Column displacement

For an easier comparison of results to experimental tests, it is convenient to establish a relationship between the column force (P) and the displacement (Δ) based on the rotational spring stiffness (k_ϕ).

The column force is calculated based on the length from the support to the periphery of the column web panel (L_c):

$$P = \frac{2M_{Ed}}{L_c}$$

The rotational spring has been chosen to act in the center of the connection as depicted in Figure 13. Furthermore, the beam is included in the stiffness model to account for the additional flexibility due to beam deflection.
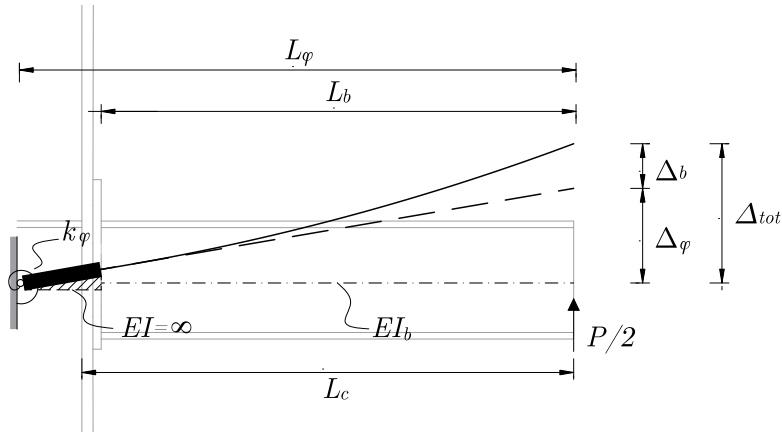

Figure 13: *Static system showing one side of the two-sided connection.*

The total displacement (Δ_{tot}) is calculated according to linear beam theory. Shear deformations are neglected.

$$\Delta_{tot} = \Delta_\phi + \Delta_b = \frac{PL_\phi^2}{2k_\phi} + \frac{PL_b^3}{6EI_b} \tag{12}$$

The force-displacement relationship obtained is shown in Figure 14, where beam span is identical to the experimental test setup described in Section 5.1.
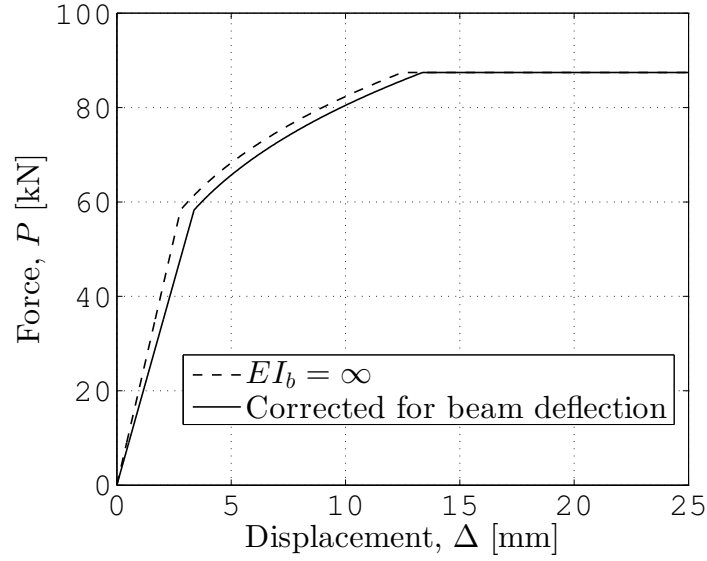

Figure 14: *Force - displacement based on Eurocode's stiffness model.*

An additional column displacement of 1 mm at maximum load is added due to beam deflection, softening the response slightly. The maximum load carrying capacity (P) is calculated to be 87 kN.

4 Material tests

A material test program was initiated to determine the mechanical properties of all the components in the connection studied in the experimental test program (Figure 3). The goal was to calibrate the necessary parameters in the rate-dependent plasticity model presented in Section 2.2.

4.1 Experimental program

Tensile tests under quasi-static conditions were performed for flange, web, plates and bolts.

Tests at increased strain rates were conducted on a selected set of the components to capture the rate-dependent behavior of the structural steel (S355) and bolt material (M16-8.8). Tests at low and medium strain rates were conducted in a servo hydraulic test machine, capable of imposing strains at 0.1 s^{-1}. The Split-Hopkinson tension bar test [20] was performed for specimens at high strain rate at approximately 100 s^{-1}.

Replicate tests were performed for each specimen for validation purposes.

4.2 Quasi-static tensile tests

Test coupons

Rectangular coupons were taken from web, flange and plate material in longitudinal and transverse directions, while circular coupons were lathed from bolts as illustrated in Figure 15.
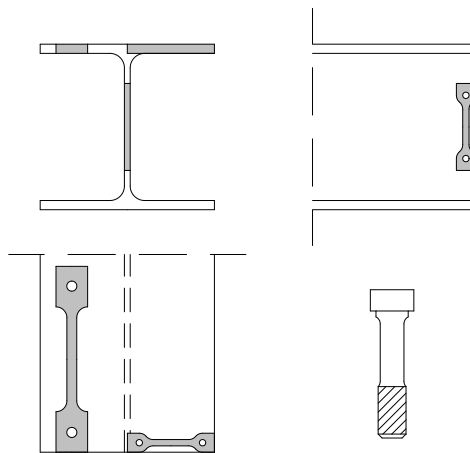

Figure 15: *Test coupons used in the material test program.*

19

All the test specimens were carefully measured by a digital apparatus before testing. Maximum deviation from nominal geometry was found to be 0.5 mm.

Loading apparatus and instrumentation
Two high resolution cameras were aligned perpendicular to the width and thickness surface for the rectangular coupons as shown in Figure 16. The cameras were calibrated to track movement in three dimensions for the circular coupons.
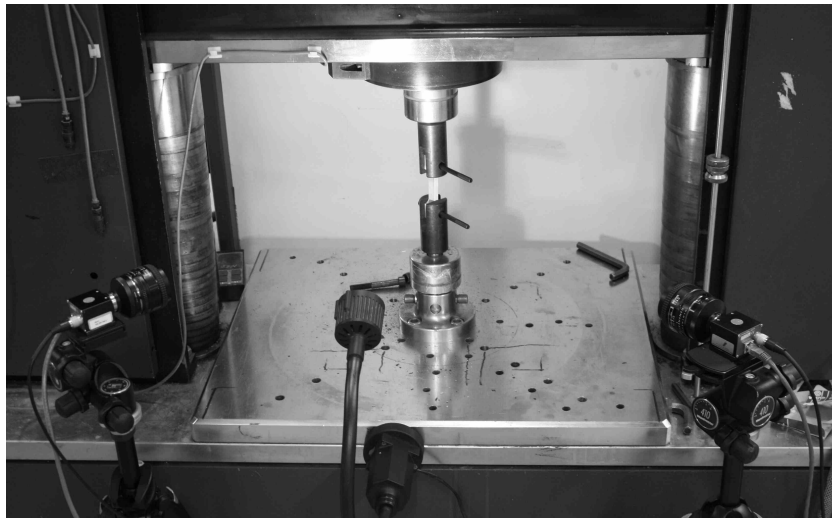

Figure 16: *Quasi-static tensile test setup.*

The specimens were pulled in tension by the actuator at a constant speed corresponding to a strain rate of 10^{-3} s^{-1}. Reaction force (F) was synchronized with pictures taken by the cameras and collected at a frequency of 1 Hz.

Digital image correlation (DIC)
DIC analysis was performed to determine the width (w), thickness (t) and longitudinal displacement (ΔL) through the use of eCorr V3.0 [21].

Cross sectional area was simply calculated as $A = w \cdot t$ for rectangular test specimens. Positional tracking in three dimensions was performed on the circular specimens as shown in Figure 17. A least square fit to a 3D circle in the neck region could therefore be used to find the cross sectional area for the circular specimens.
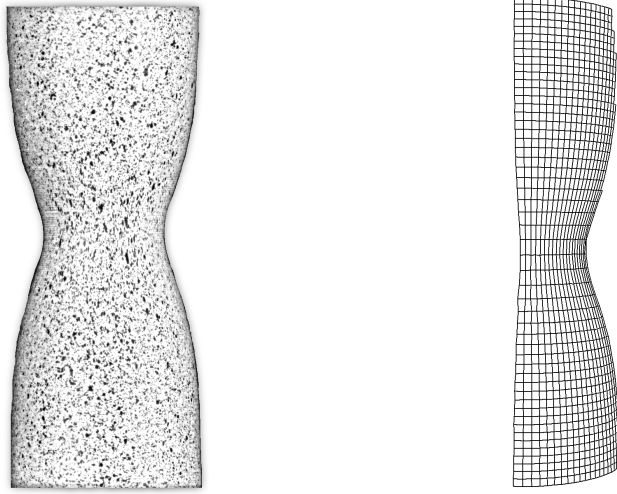
Figure 17: *DIC analysis of circular coupon. Bitmap image (left) and 3D mesh (right).*

4.3 Work hardening

As discussed in Section 2.3, simple finite stress-strain relations can not be obtained from tensile test during necking in a specimen. Inverse modeling was therefore used to quantify the isotropic work hardening function (R) defined in Eq. (5).

Self Consistent Method
Before neck initiation, equivalent stress and strain were calculated from the test data using Eq. (9a) and Eq. (9b). During necking, average axial stress and strain were obtained from Eq. (10a) and Eq. (10b). Finally, the triaxial stress correction function (ζ) defined in Eq. (11) was found by a self consistent trial and error method established by Yazzie et al. [16].

The basic principle behind the Self Consistent Method is the use of finite element simulations to iteratively seek the stress correction function which best fit the experimental data. A simple flow chart can be seen in Figure 18.
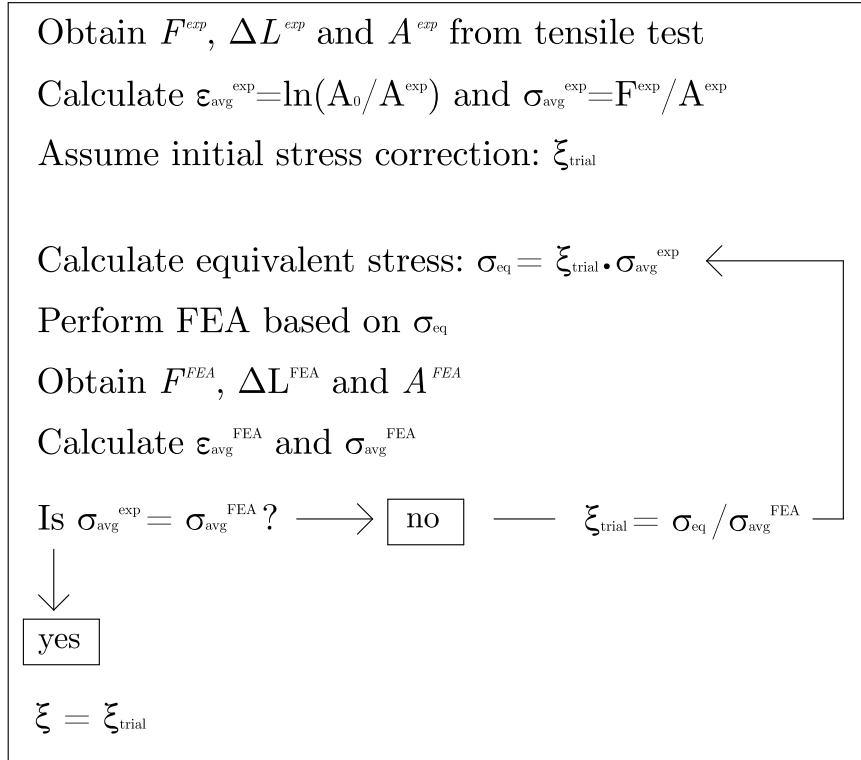
Obtain F^{exp}, ΔL^{exp} and A^{exp} from tensile test

Calculate $\varepsilon_{avg}{}^{exp} = \ln(A_0/A^{exp})$ and $\sigma_{avg}{}^{exp} = F^{exp}/A^{exp}$

Assume initial stress correction: ξ_{trial}

Calculate equivalent stress: $\sigma_{eq} = \xi_{trial} \cdot \sigma_{avg}{}^{exp}$ ⟵

Perform FEA based on σ_{eq}

Obtain F^{FEA}, ΔL^{FEA} and A^{FEA}

Calculate $\varepsilon_{avg}{}^{FEA}$ and $\sigma_{avg}{}^{FEA}$

Is $\sigma_{avg}{}^{exp} = \sigma_{avg}{}^{FEA}$? ⟶ no — $\xi_{trial} = \sigma_{eq}/\sigma_{avg}{}^{FEA}$

↓

yes

$\xi = \xi_{trial}$

Figure 18: *Flow chart of the Self Consistent Method.*

Two symmetry planes were utilized in modeling of the test coupons, and a very small initial imperfection was added to initiate necking. A typical finite element model showing the mesh density used in calibration is shown in Figure 19.
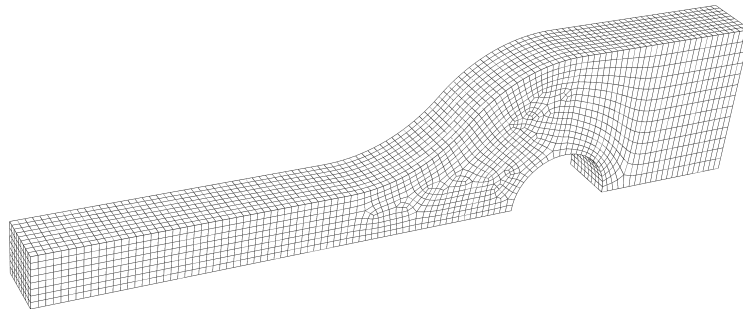
Figure 19: *Typical finite element model used in the Self Consistent Method.*

22

Three iterations were usually sufficient for each test coupon and gave the material curves shown in Figure 20. A minor scatter in the structural steel material (S355) is observed between web, flange and plate specimens.
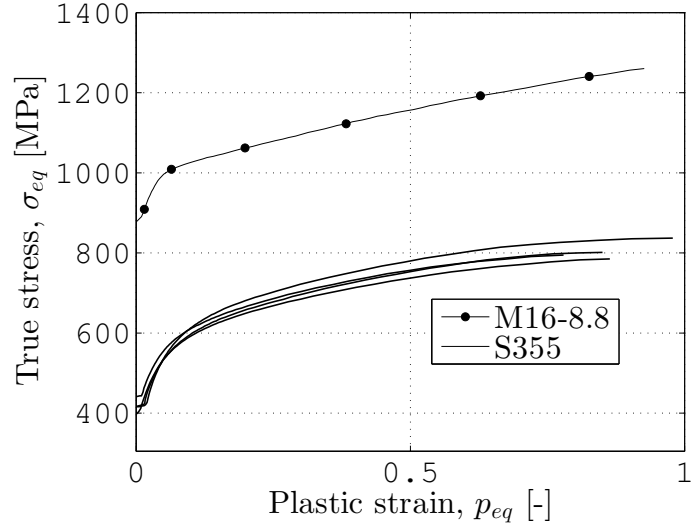

Figure 20: *Work hardening curves obtained by the Self Consistent Method.*

Validation

In order to assess the Self Consistent Method's ability to simulate the material behavior, the tensile test simulations are compared to the experimental tests in Figure 21.
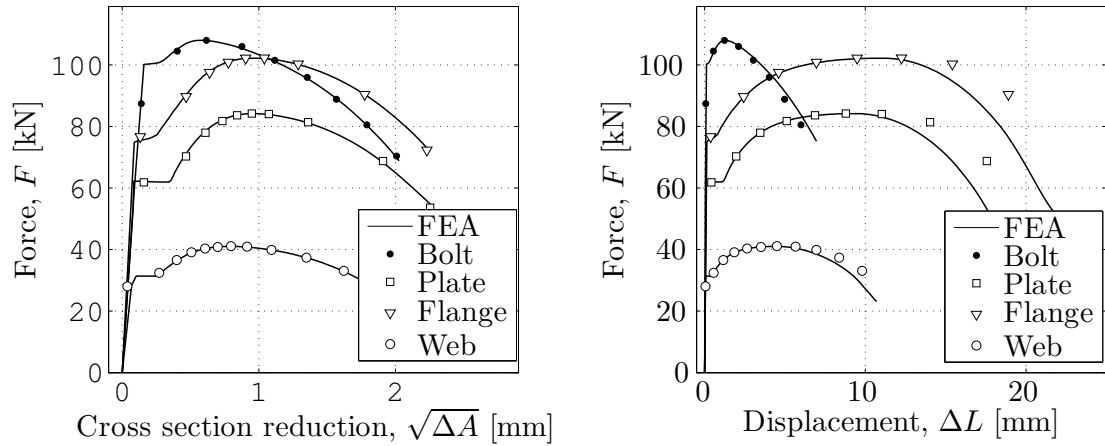

Figure 21: *Self Consistent Method compared to tensile test results.*

23

A good fit is observed until neck initiation (maximum load), after which longitudinal displacement starts to deviate from the experiment. However, the reduction in cross section is simulated accurately until fracture.

This behavior can be explained by considering the underlying principle of the Self Consistent Method, which is the calibration of average stress ($\sigma_{avg} = F/A$), and not the engineering stress ($s = F/A_0$).

According to studies done by Khoo et al. [22], cross sectional reduction is a more accurate comparison approach. It is therefore concluded that the Self Consistent Method gives satisfactory results.

Mesh dependence

Mesh dependence in the finite element models has been studied by varying the element size in the dog-bone specimen shown in Figure 19.
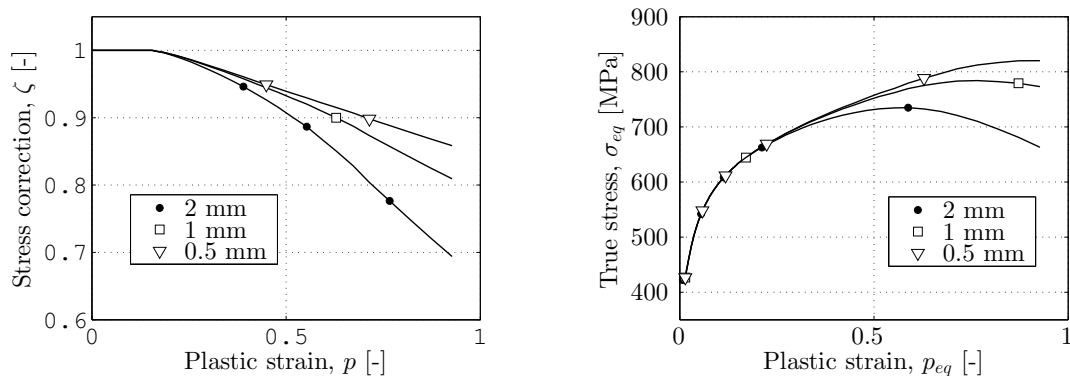
Figure 22: *Effect of changing the element size on a rectangular dog-bone specimen.*

As Figure 22 indicates, the hardening curves obtained show a strong mesh dependence. Mesh refinement does not seem to give a converging solution; decreasing the element size will increase the equivalent stress. Mesh size dependence is therefore expected in the use of the hardening curves in a finite element simulation.

4.4   Rate sensitivity

Additional tension tests were performed at four different strain rates in order to determine the viscous material behavior. The flow stress was found to increase as shown in Figure 23.
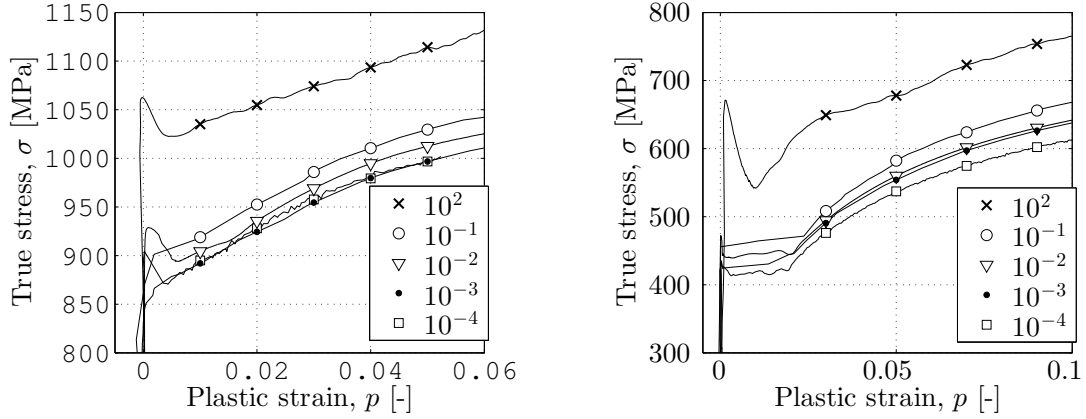
Figure 23: Stress at elevated plastic strain rates for M16-8.8 (left) and S355 (right).

Calibration method

The viscous exponent (c) determining the rate-dependent yield behavior in the constitutive model was calibrated from the test data. By considering the viscous stress defined in Eq. (6):

$$\sigma_{eq} = (\sigma_0 + R)(1 + \frac{\dot{p}}{\dot{p}_0})^c$$

and taking the logarithm:

$$\log\left[\frac{\sigma_{eq}}{(\sigma_0 + R)}\right] = c \cdot \log\left[1 + \frac{\dot{p}}{\dot{p}_0}\right]$$

reveals that the viscous exponent can be found as the slope of the curve in a log-log plot shown in Figure 24. A reference strain rate $\dot{p}_0 = 0.01$ s^{-1} was used.
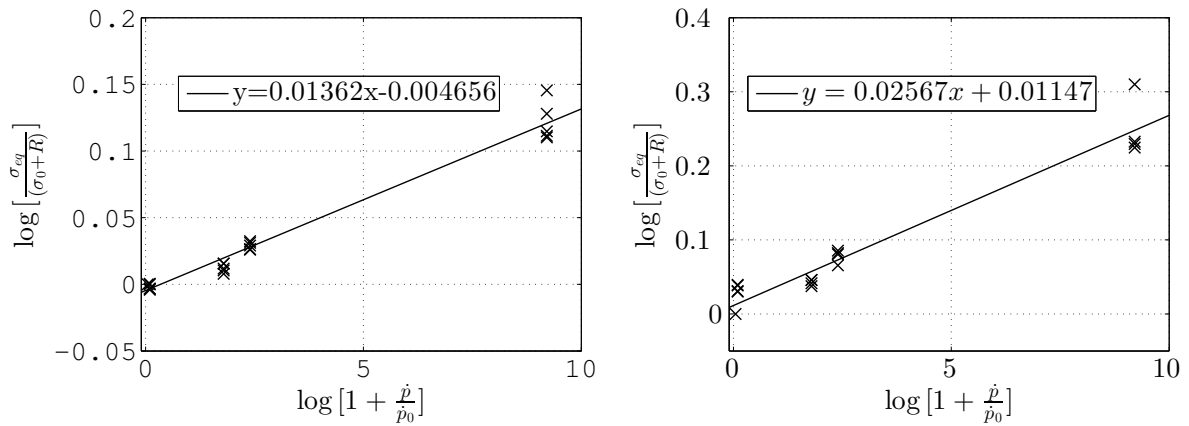
Figure 24: Least square fit of the viscous exponent for M16-8.8 (left) and S355 (right).

4.5 Fracture

The Cockcroft and Latham fracture criterion (W_c) defined in Eq. (7) was calibrated from tensile tests performed under quasi-static conditions. Fracture energy was found not to be strongly dependent on strain rate for low and medium strain rates below 0.1 s^{-1}.

Calibration method

The total energy absorbed by the specimen is given as:

$$E = \int_0^{u_f} F \cdot du$$

where u_f is the axial displacement at fracture. Fracture was defined when the energy obtained by finite element simulation matched the experiment:

$$E^{FEA} = E^{exp}$$

The critical strain energy per unit volume was then found by integrating principal stress and strain at integration points for all the elements in the critical section:

$$W_c = \int_0^{\varepsilon_f} max(\sigma_1, 0) d\varepsilon_1$$

As illustrated in Figure 25, the principal stress is greater for elements at the center of the specimen due to triaxiality. The fracture criterion (W_c) will therefore vary over the thickness of the specimen.
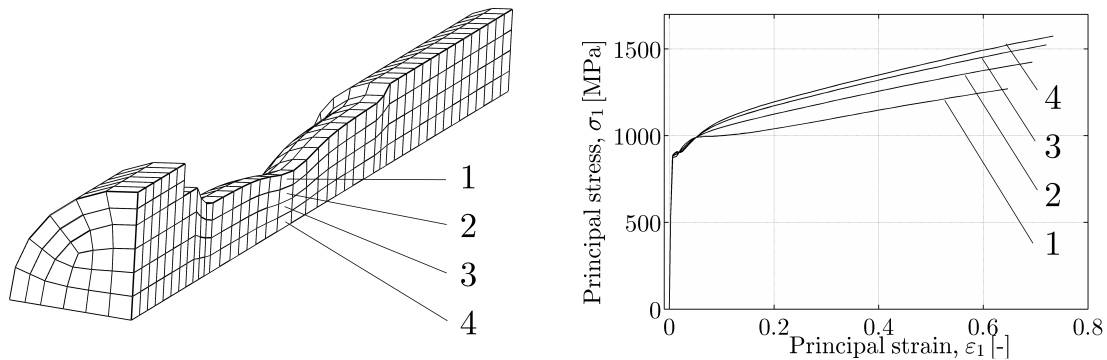

Figure 25: *Principal stress for elements over the thickness in critical section.*

In addition, the fracture strain (ε_f) will be strongly dependent on the element size; a finer mesh will increase the local straining of an element. Due to such element size dependencies, the same mesh density as used in simulations (Section 6) was used in the calibration.

The results can be seen in Table 3. Note that the scatter is because of the triaxial stress state in the neck region.

Table 3: *Scatter in Cockcroft and Latham fracture criterion*

	W_c [Nmm^{-2}]
M16-8.8	713 - 954
S355	554 - 611

5 Experimental tests of joints

Experimental tests were carried out to investigate the behavior of the joint shown in Figure 3 in a column removal scenario.

Load scenarios

Monotonic displacement of the column due to loss of vertical support is the basis of the quasi-static loading conditions and serves as a reference for the dynamic experiment.

The scenario behind the dynamic experiment is a sudden impact by a falling object, with kinetic energy corresponding to a one story drop of a 400 kg mass.

Specimens

Quasi-static and dynamic experiments have been conducted on the specimen shown in Figure 26.
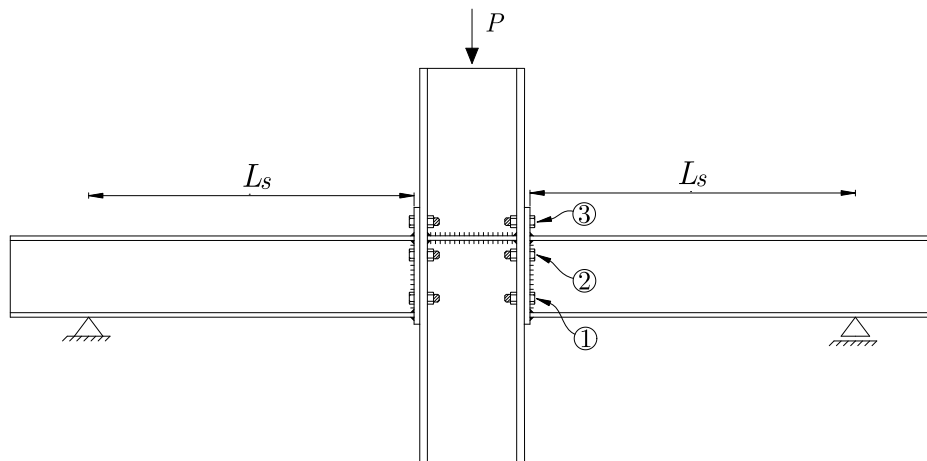
Figure 26: Experimental test specimen.

A torque wrench was used to tighten the bolts with a moment of 80 Nm to ensure contact between the end-plate and the column flange.

The geometry of the assembled connections was measured by a tape measure. Maximum horizontal deviation between end-plate and column flange was found to be 3 mm. The thickness of the end-plate deviated from nominal values by 1 mm.

5.1 Quasi-static experiment setup

Setup and loading

The test specimen was placed in an upside-down position under a portal frame structure depicted in Figure 27. For additional pictures, see Figure C.56.

Steel angles with a circular support surface were placed loosely between the portal beam and the specimen. The beam span (L_s) defined in Figure 26 was measured to be 685 mm.

A 1000 kN hydraulic actuator pulled the column end upwards at a constant speed of 0.05 mm/s. The experiment was stopped after failure was observed on one side of the connection.
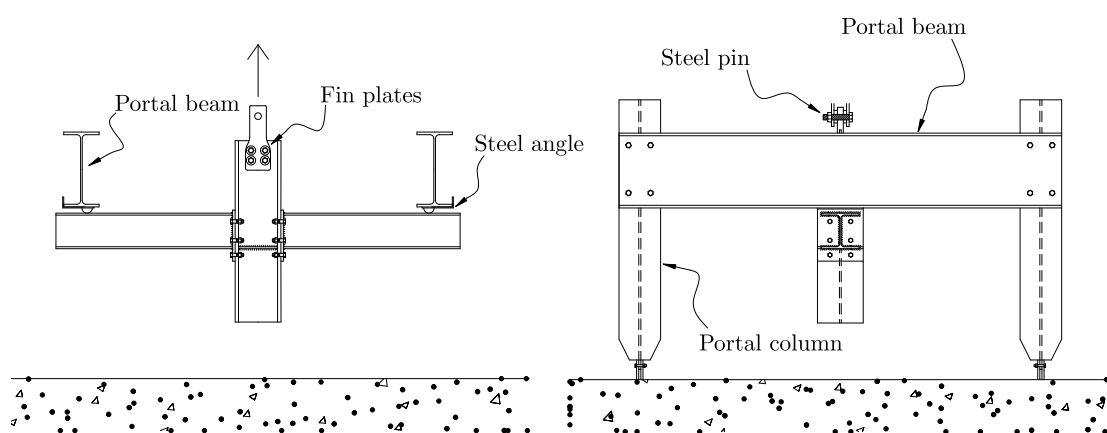
Figure 27: Setup for quasi-static experiment.

Instrumentation

A linear variable differential transformer (LVDT) was used to measure the displacement of the column end relative to the floor. Additional LVDT's were placed under each support in order to correct for any deflections in the portal beams.

Strain-gauges placed onto the column web and the beam flanges were primarily used to assess the degree of symmetry during loading.

Two cameras were calibrated to perform three dimensional position tracking of the central part of the connection using DIC analysis.

5.2 Dynamic experiment setup

Setup and loading

A pendulum impactor (kicking machine) was used in the dynamic crash tests [23].

It consists of an arm that swings around a bearing, which is accelerated by an hydraulic piston at one end and attached to a trolley at the other end. The moving trolley is then guided on rails into a direct impact with the specimen.

The specimen was placed in a vertical position next to an extended support structure, which was bolted to a concrete reaction wall as shown in Figure 28. Additional pictures of the setup are shown in Figure C.57. Steel forks were used to restrict any lateral beam movements. A 20 mm thick steel plate was taped to the column end in order to distribute impact forces.

The horizontal offset of the impactor relative to the centerline of the column was 7 mm. The beam span (L_s) defined in Figure 26 was measured to be 687 mm.
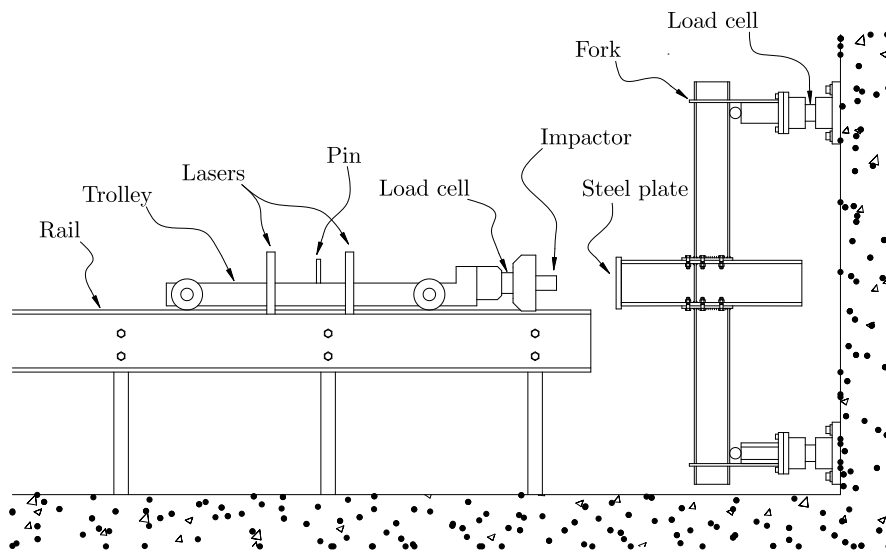

Figure 28: *Setup for dynamic experiment.*

The trolley with a total mass of 726.7 kg was accelerated on the rail system up to a speed of 6.02 m/s by the kicking machine.

Instrumentation

A load cell on the trolley was used to measure the impact forces. A second load cell was recording the reaction forces at the upper support.

A laser device was continuously measuring the distance of the trolley relative to the reaction wall during the experiment. Velocity and acceleration were calculated by numerical differentiation, and allowed for a validation of the load cell by multiplying acceleration by the mass of the trolley.

One camera was used to capture local displacement in the central region of the joint using DIC. A second camera was capturing a wider view of the specimen, including the extended support structure.

5.3 Quasi-static results

General observations and failure mode
Two identical experiments were conducted for validation purposes. Experiment 1 failed due to thread stripping in bolt row ①. A second nut was therefore added in experiment 2 to allow for full utilization of the net section capacity.

A flexural behavior with bending of the end-plate and elongation of the bolts in row ① lead to failure as shown in Figure 29. A simple visual inspection reveals that the plate opening remained closed in the position of bolt row ②.
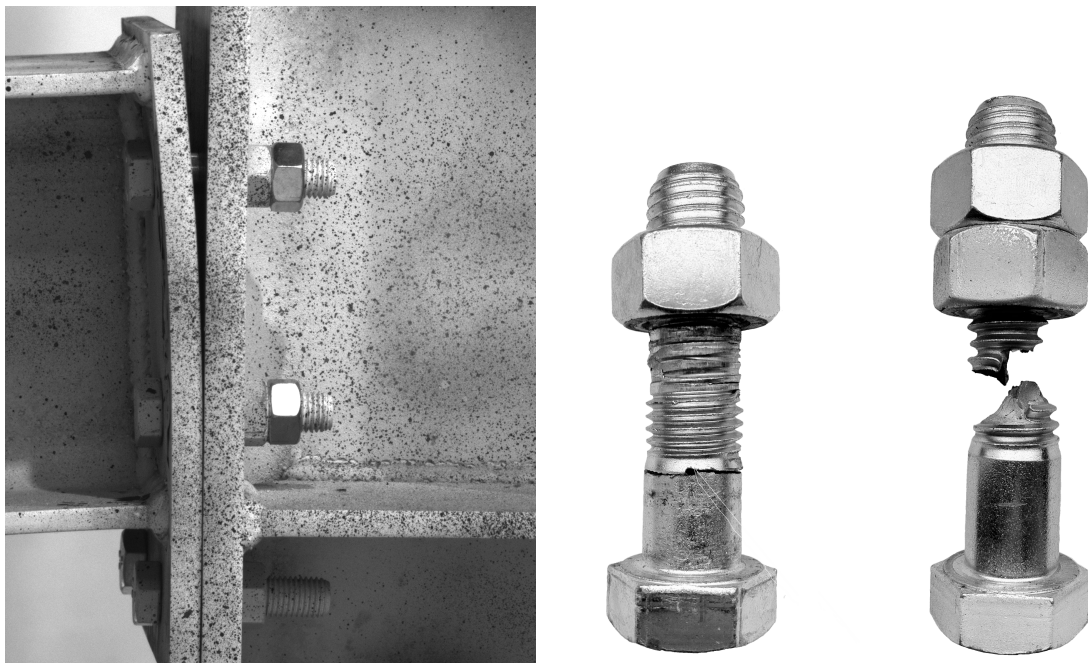
End-plate opening at time of fracture in experiment 2.

Thread stripping (left) and tensile fracture (right).

Figure 29: *Pictures of quasi-static tests.*

Some plastic deformation of the end-plate was observed after unloading, while the column flange remained in the elastic range.

In retrospect, it is questioned whether the steel angles with the circular support surface (see Figure 27) could have moved outwards during the experiment due to

31

friction, lengthening the beam span. Unfortunately, this was not actively observed during the experiment or measured afterwards, leaving the issue unresolved.

Displacement measurements
The vertical column displacement is presented in Figure 30. The initial stiffness is similar for the two experiments, with a gradual reduction due to plastification of the end-plate and the bolts. Maximum column load (P) measured by the actuator was 138 kN.
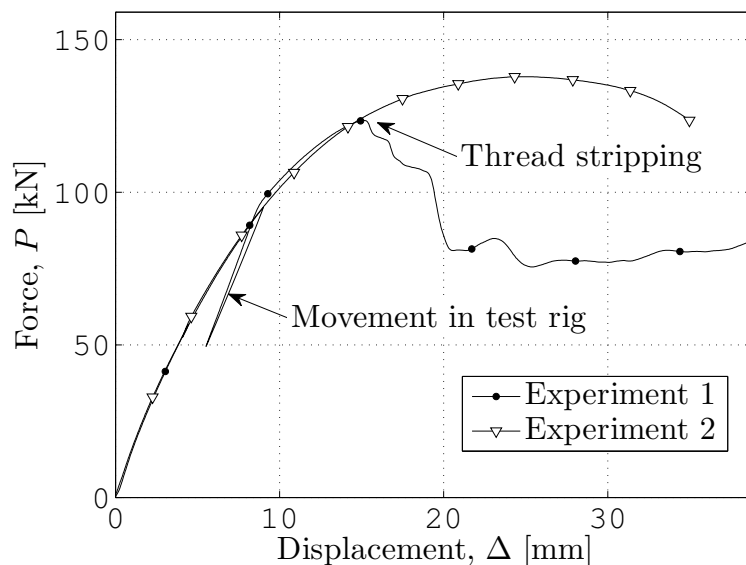

Figure 30: *Column force and displacement in quasi-static experiments.*

5.4 Dynamic results

General observations and failure mode
Unfortunately, a replicate test had not been performed at the time of writing this thesis. It is therefore difficult to assess the degree of randomness in the obtained results.

The trolley impacted and caused a flexural behavior with an opening of the end-plate which ultimately lead to tensile fracture in bolt row ① as shown in Figure 31.
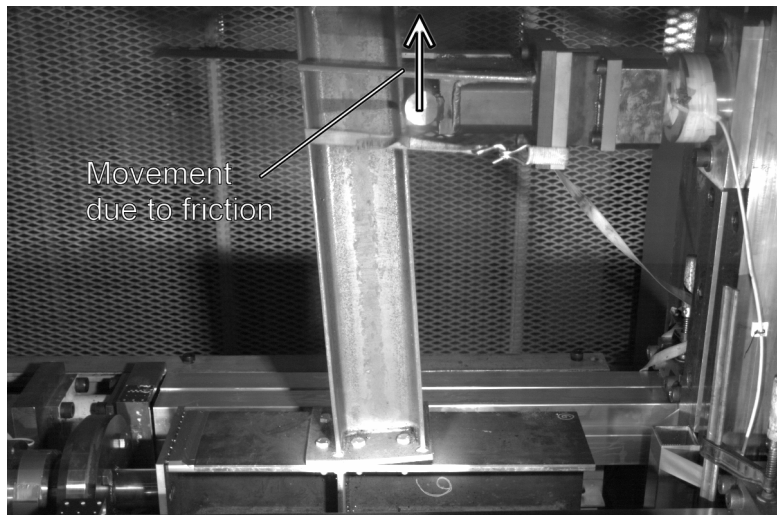
Careful observations of the high speed camera footage revealed that the support structure moved upwards due to friction between the support and the beam specimen, which was estimated to be approximately 10 mm.
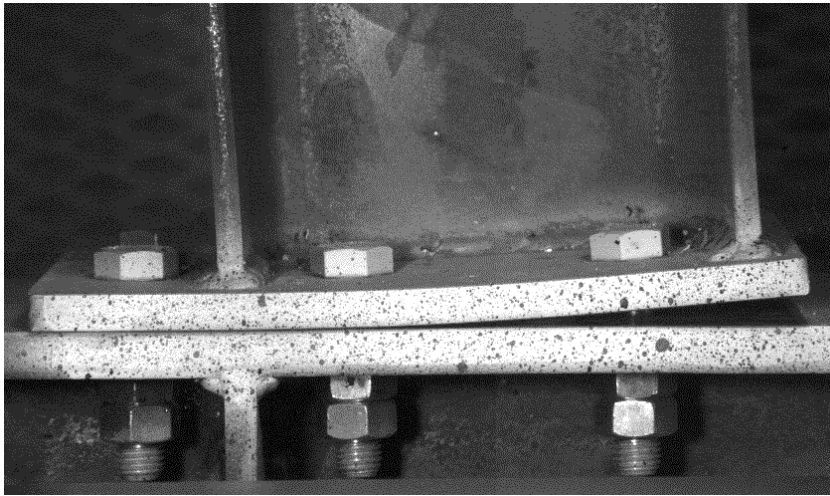
End-plate opening at time of fracture.   *Tensile fracture.*

Movement
due to friction

Support structure at time of fracture.

Figure 31: *Pictures of dynamic test.*

Force measurements

A closer look at the force measurements reveals that the specimen was hit by the impactor in a series of elastic collisions as shown in Figure 32. Each collision lasted about 1 ms and transfered short impulse forces of 1200 kN, which is approximately 10 times that of the quasi-static experiment.

After the initial collision, a 2 ms delay is observed before any reaction was registered at the support. Afterwards, the beam started to oscillate with a period
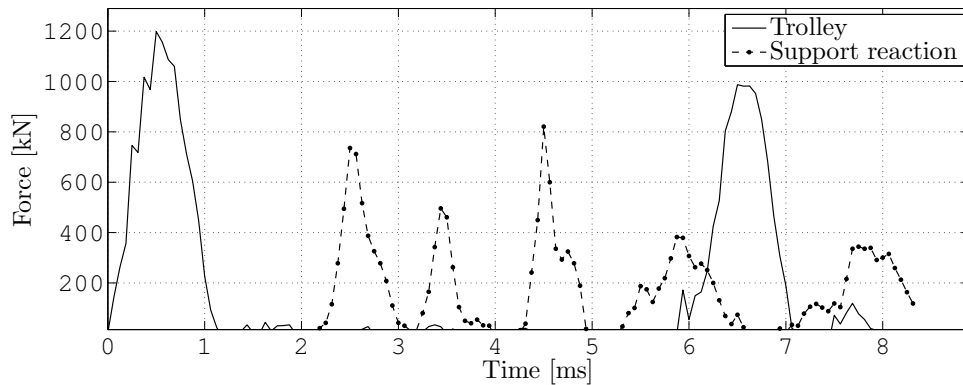
of about 1 ms.

Figure 32: *Force measurements in dynamic experiment showing a 2 ms delay from initial impact to support reaction.*

Comparing quasi-static and dynamic results

The general response characteristics did not change in the dynamic experiment. A flexural behavior and tensile fracture of bolts were compatible to findings under quasi-static conditions.

However, using DIC analysis to measure the opening of the end-plate at the position of bolt row ① reveals some minor differences. A 10 % reduction in the plate opening at time of fracture in the dynamic experiment can be seen in Figure 33.
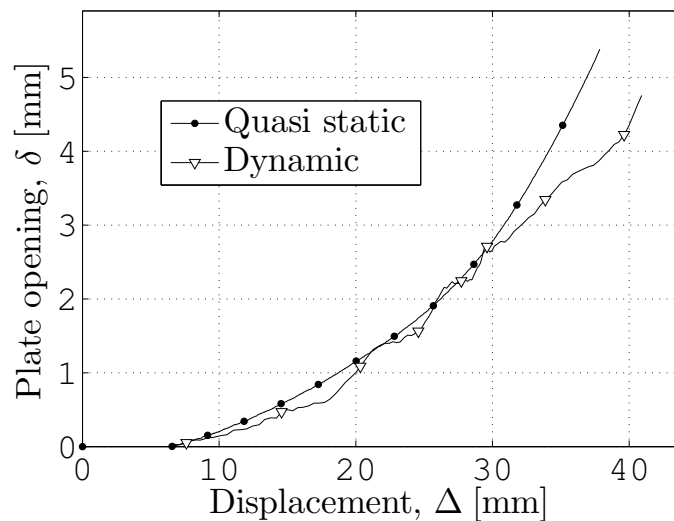

Figure 33: *Opening between end-plate and column flange at position of bolt row 1.*

34

6 Finite element simulations

Three dimensional explicit analyses have been performed in Abaqus V6.12 [24] for both quasi-static and dynamic simulations of the experimental tests discussed in Section 5. The constitutive model was implemented through SIMLab Metal Model [25].

In Section 6.1, the finite element model is presented. A great deal of assumptions were made in establishing the model. Therefore, a parametric study was carried out in Section 6.2 to investigate the effect of changing important variables. Finally, the results are given in Section 6.3 - 6.4.

6.1 Finite element model

Geometry
The nominal geometry has been used for all the parts in the assembly shown in Figure 34. Local buckling of column web in compression is assumed to be restricted by the stiffener, and two symmetry planes were utilized in order to reduce the computing time. No initial imperfections in the geometry were used.
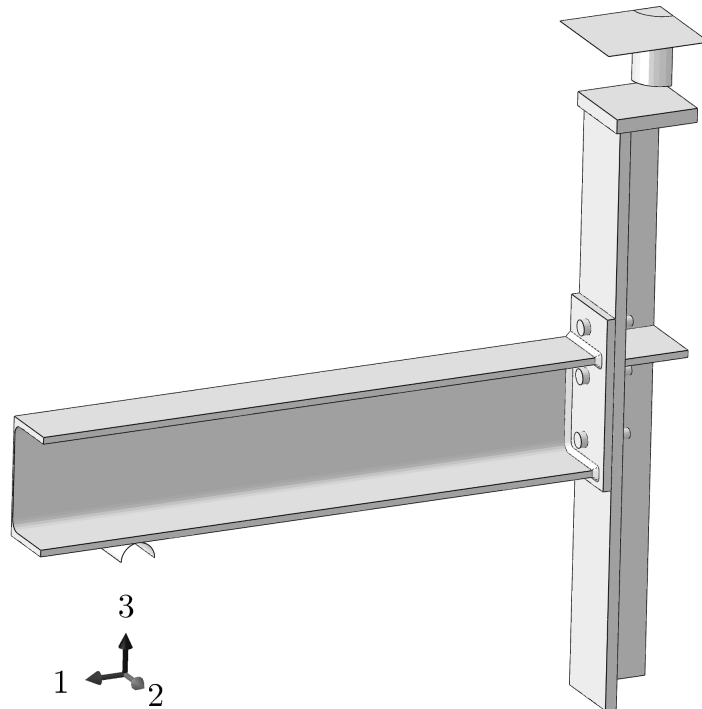

Figure 34: *Model geometry showing quarter symmetry, rigid support and trolley with impactor (top).*

The trolley has been modeled as a rigid plate with a point mass, while the impactor is modeled as a deformable solid. The mass of the trolley and the impactor correspond to one quarter of the total measured mass of 726.7 kg.

The bolt head, shank and nut have been modeled as one solid part as shown in Figure 37. The threaded region of the shank is idealized as circular with diameter corresponding to the cross sectional area $A_s = 157$ mm^2.

Mesh

Linear brick elements with reduced integration (S4R) were used throughout. Default hourglass control was used in Abaqus for the quasi-static simulation, while viscous hourglass control was added in the dynamic simulation, which is recommended for high impact analysis [26].

A medium dense mesh was chosen after a sensitivity study covered in Section 6.2. The mesh, pictured in Figure 35, is refined around a central region of the connection for a more accurate representation of the stress field where high gradients are expected. A finer mesh was also applied to the impact region in the model used in the dynamic simulations.
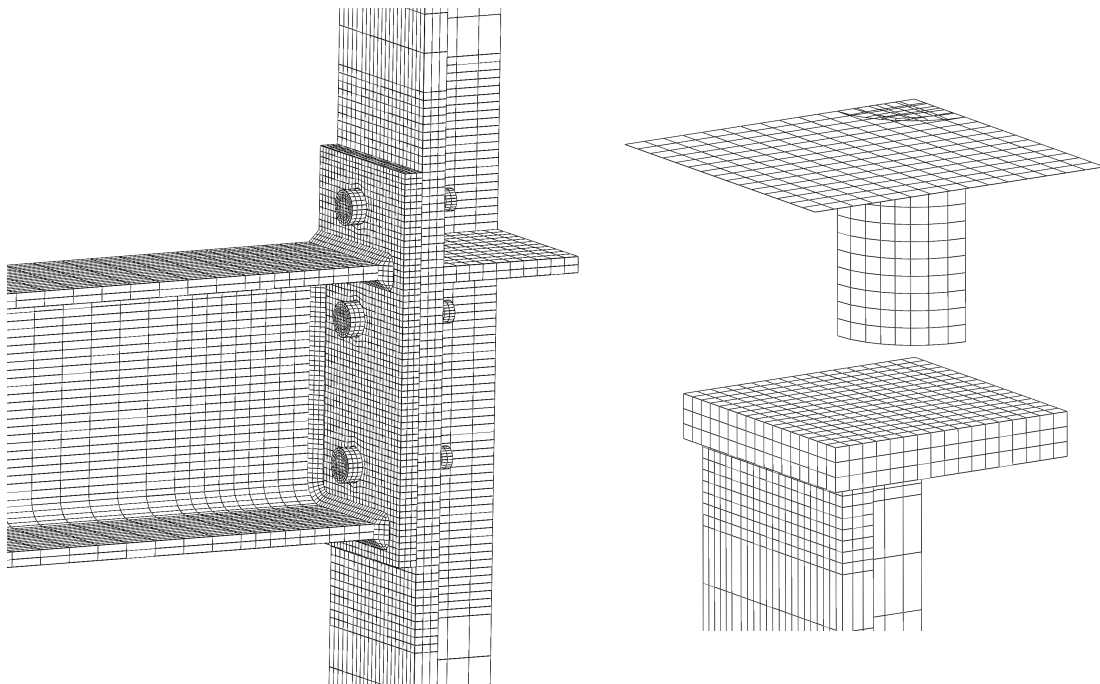

Figure 35: *Mesh used in quasi-static- and dynamic simulations (left) and dynamic simulations (right).*

36

Material

Hardening curves were found by an inverse modeling technique as described in Section 4.3, and can be seen in Figure 36. The weld material is obtained by dividing the yield stress of the plate material by a factor $\beta = 0.9$ according to NS-EN-1993 [27]. Scatter in the yield stress of the strucural steel material (S355) is accounted for by applying separate hardening curves to flange, web and plates.
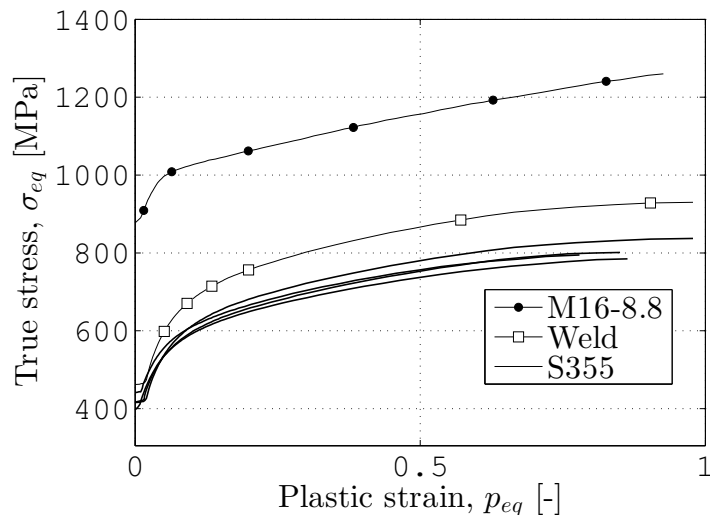

Figure 36: *Isotropic hardening used in the plasticity model.*

Physical properties of steel assumed to be representative for all materials used are given in Table 4. Additional material parameters describing the viscous stress (c) and fracture (W_c) are listed in Table 5. Note that an average value has been chosen for the fracture criterion, which was found to vary over the thickness as discussed in Section 4.5.

Table 4: *Physical constants [27]*

E [MPa]	ν [-]	ρ [kg m^{-3}]
210000	0.3	7800

Table 5: *Material parameters*

|	$\dot{p}_0$ [s^{-1}]	c [-]	W_c [N mm^{-2}]
M16-8.8	0.01	0.01362	834
Weld	0.01	0.02567	648
S355	0.01	0.02567	583

Interactions

The geometry is divided into sub-assemblies using tie-constraints as shown in Figure 37. A general contact formulation with finite sliding is used in Abaqus for interaction between them. The friction coefficient is taken as $\mu = 0.2$ for untreated steel surface according to NS-EN-1090 [28].
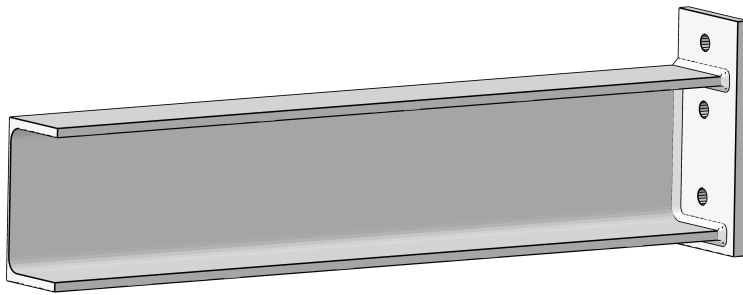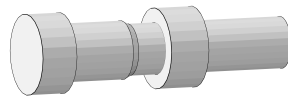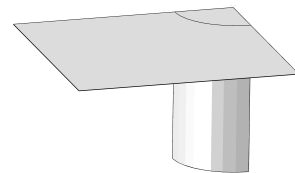
Beam with welded end-plate.
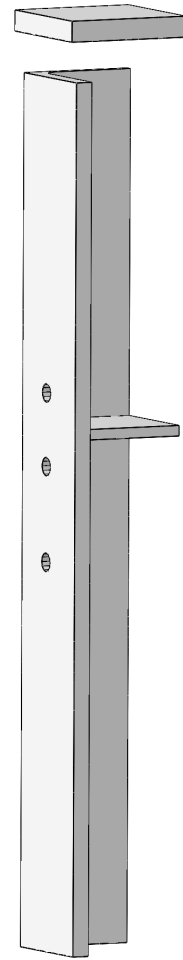
Column with stiffener.
Force distributor (top).
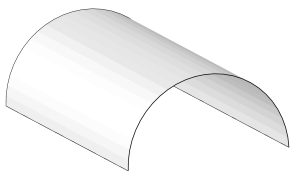
Rigid support.

Bolt.

Trolley (rigid plate) with
impactor.

Figure 37: *Sub-assemblies used in the finite element model. Trolley with impactor and force distributor are not used in quasi-static simulations.*

Special attention has been payed to the contact conditions at the support. A sensitivity study described in Section 6.2 revealed that spurious reaction forces may develop. Contact without friction has therefore been chosen between the support and the beam flange.

Boundary conditions
Quarter symmetry (see Figure 34) is obtained by xz- and yz symmetry planes, which restricts movement in y and x direction respectively. A fixed boundary condition is placed on the support, while the trolley traveling on rails is restricted from moving in x- and y direction.

Loading conditions
A constant velocity of 0.5 m/s was applied to the column end in the quasi-static simulation. The velocity was applied smoothly to reduce oscillations that occur when motion is introduced suddenly in an explicit analysis. The initial velocity of the trolley was set to the measured value of 6.02 m/s in the dynamic simulation. The applied velocities are illustrated by the arrows in Figure 38
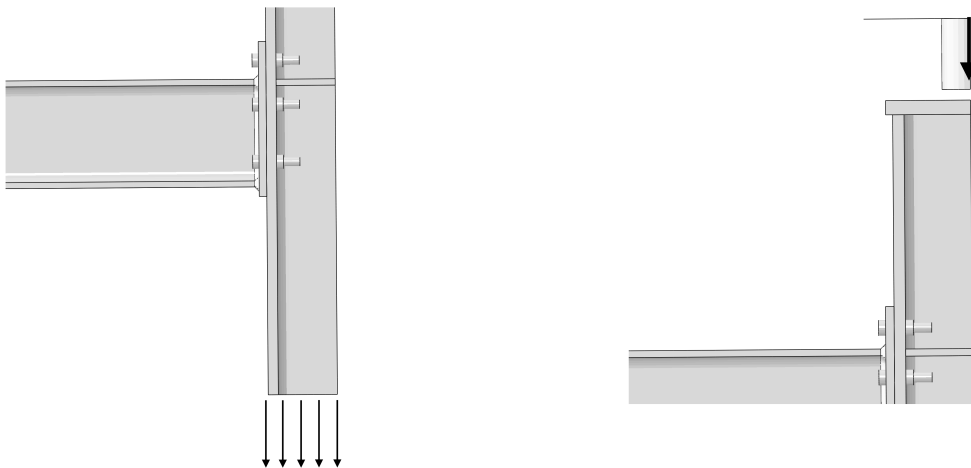

Figure 38: Velocity conditions used in quasi-static simulation (left) and dynamic simulation (right).

Special attention needs to be given to explicit analysis under quasi-static conditions. A real time scale is generally not possible due to very small time steps needed in explicit time integration. Examinations revealed that the kinetic energy was below 1 % of the internal energy, indicating that conditions were in fact quasi-static.

6.2 Sensitivity

A series of simulations have been conducted in order to discover sensitivities in the finite element model. The focus has been on a few parameters that are considered to have a relatively large impact on the results.

Element size

Hardening curves are obtained by the use of an inverse modeling technique as described in Section 4.3. A very fine mesh was used in material calibration, and element size dependence in the global analyses was therefore expected.

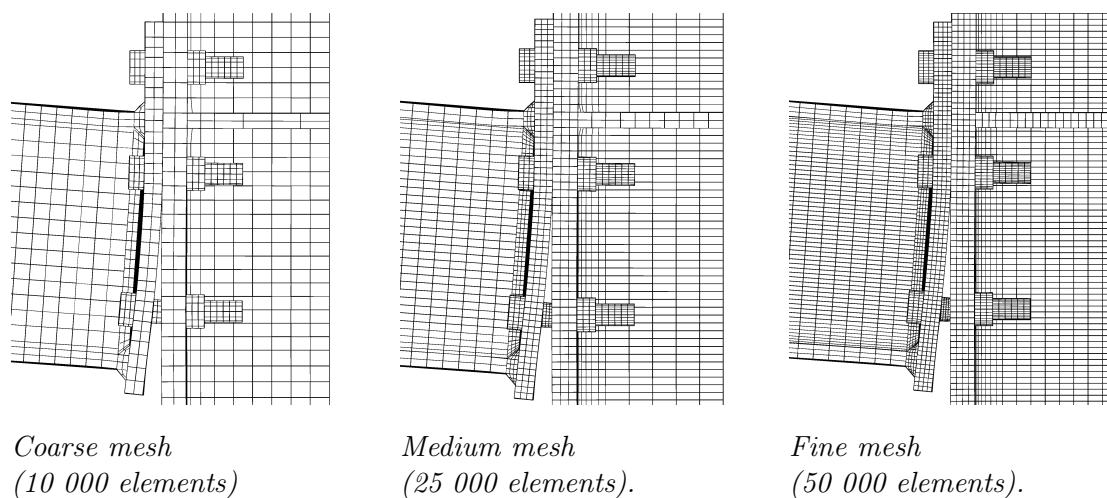A coarse, medium and fine mesh was created as seen in Figure 39.

Coarse mesh
(10 000 elements)

Medium mesh
(25 000 elements).

Fine mesh
(50 000 elements).

***Figure 39:** Different element mesh used in sensitivity simulations.*

Both quasi-static and dynamic simulations were performed. The results can be seen in Figure 40. A medium dense mesh appears to provide a converging solution.
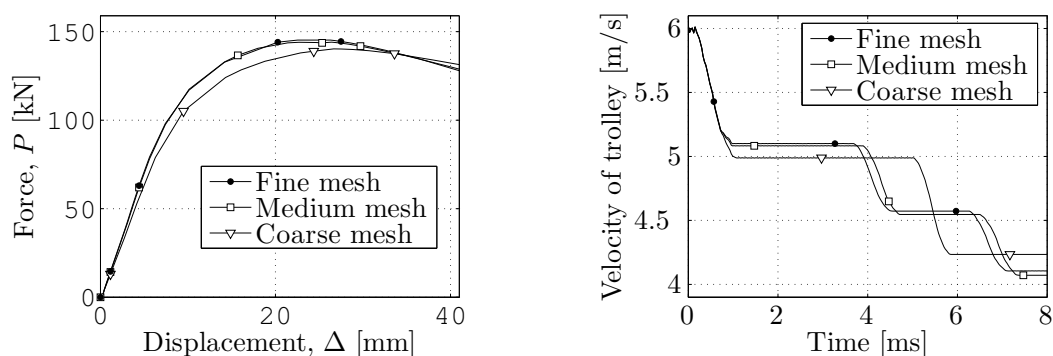

***Figure 40:** Mesh convergence of quasi-static (left) and dynamic simulation (right)*

Prestress of bolts

The importance of applying an initial stress state to simulate the tightening of the bolts to a moment of 80 Nm in the experimental tests has been investigated.

The axial bolt load is calculated according to NS-EN-1090 [28]:

$$F = \frac{M}{k \cdot d} = \frac{80\text{Nm}}{0.13 \cdot 16\text{mm}} = 40\text{kN}$$

where k is assumed to be the mean value of the valid range of $0.10 - 0.16$ according to NS-EN-14399 [29].

Quasi static simulations have been conducted for an assembly with and without prestressed bolts. The results can be seen in Figure 41.
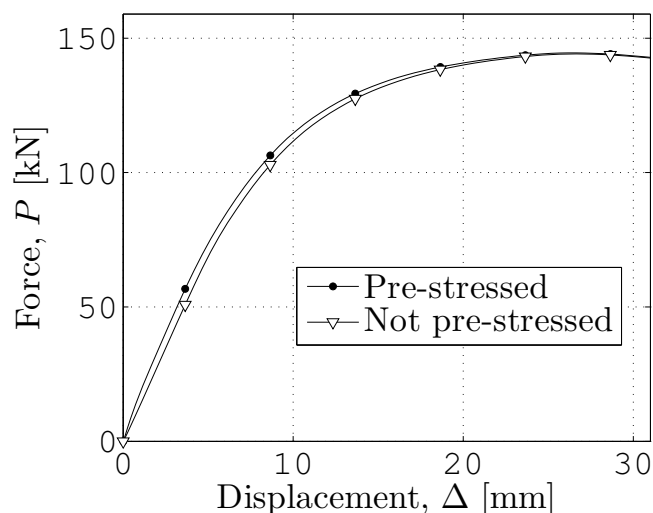

Figure 41: *With and without prestressed bolts (40 kN).*

The assembly with prestressed bolts shows a slightly greater initial stiffness without any change in maximum load, in effect translating the force-displacement curve horizontally. It is therefore concluded that the model is not heavily dependent on the prestress.

Beam span

The initial length to the support was measured carefully before the experimental test, but was observed to be lengthening (aproximately 10 mm) due to frictional forces between the specimen and the support as discussed in Section 5.4. Therefore it is interesting to study the effect of changing the beam span in the finite element model.

Simulations have been conducted under quasi-static conditions with a shortening and lengthening of the distance to support by 15 mm. The results can be seen in Figure 42.
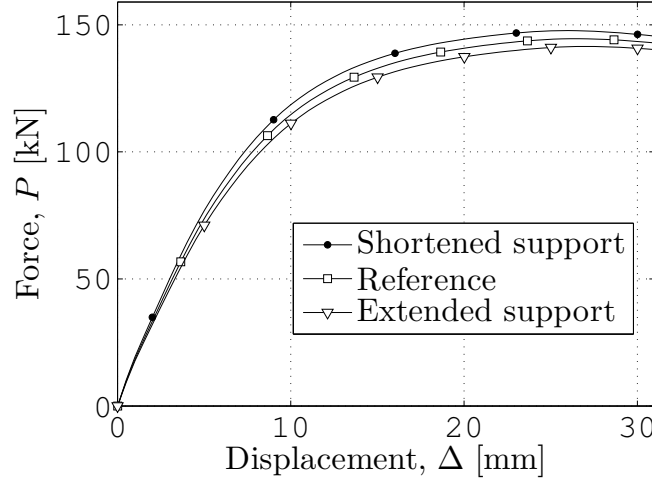

Figure 42: *Length to support (685 ± 15 mm).*

An increase of 15 mm correspond to a 2 % change in maximum force and a softer response. The opposite is observed when the distance is shortened. This behavior can be explained by considering the cross sectional moment:

$$M = \frac{P}{2} \cdot (L_s \pm \Delta L_s)$$

An increase in the distance to the support will reduce the load:

$$P = \frac{2M}{L_s \pm \Delta L_s}$$

$$\frac{P}{P_0} = \frac{L_s}{L_s \pm \Delta L_s} = \frac{685}{685 \pm 15} = 1.00 \pm 0.02$$

The 2 % change can therefore be explained by considering the cross sectional moment. The uncertainty in force can be as much as 1-2 % when compared to the experimental results.

Friction

A change in the friction coefficient between the steel surfaces in the central part of the connection μ_{joint} and between the beam flange and the support $\mu_{support}$ has been investigated. The results are shown in Figure 43.
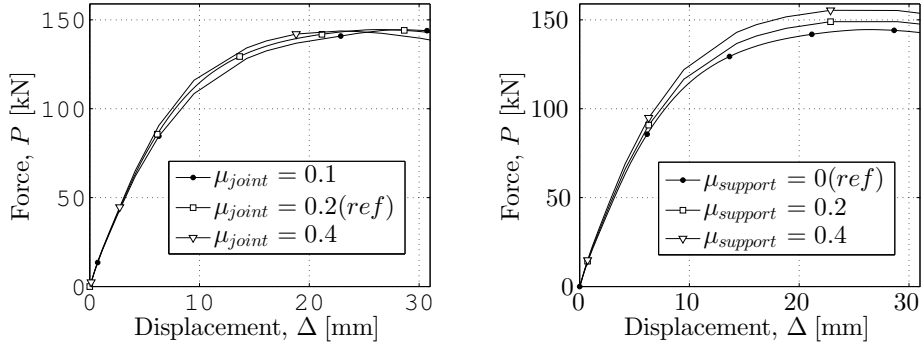
Figure 43: *Effects of changing the friction coefficient in the central region of joint (left) and at the support (right).*

Increasing the friction coefficient for central parts of the connection gives a slight increase in the initial stiffness and vice versa. The maximum load remains unaltered.

Increasing the friction coefficient at the support however will significantly change both stiffness and maximum load. Very large horizontal reaction forces and compressive axial stress in the beam may develop in the simulation. In the experimental setup, this was not the case because the support was not sufficiently fixed (see Section 5.1).

It is therefore concluded that the finite element model is sensitive to the value of friction coefficient at the support.

6.3 Quasi-static results

Response and failure mode
Bolt row ① failed in tension due to an excessive opening of the end-plate. The maximum vertical load was found to be 144 kN.

The stress state at time of failure shown in Figure 44 reveals which of the components that are active in the transfer of forces. The bending moment is primarily carried by bolt row ① in tension, with row ② not utilized beyond initial yield. The shear force is carried by bolt row ① and ②. Bolt row ③ seems not to be part of any significant load transfer.
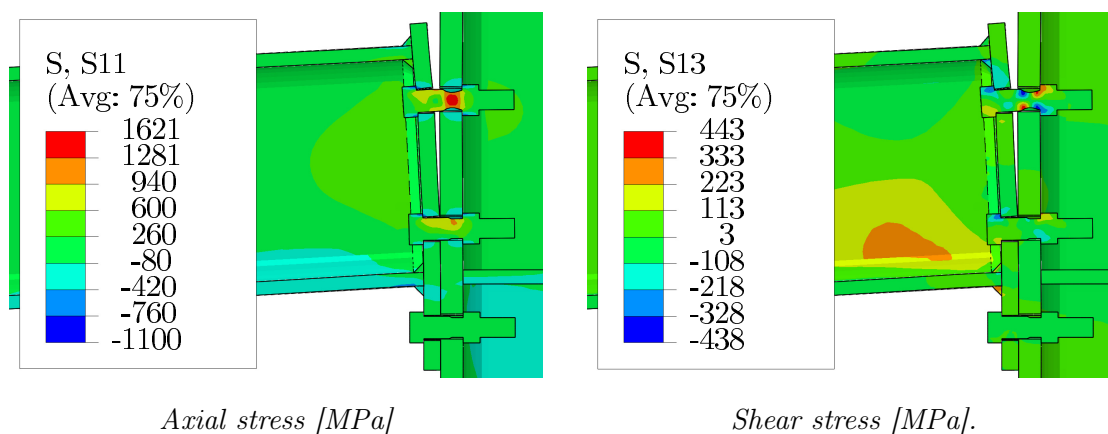
Axial stress [MPa]   Shear stress [MPa].

Figure 44: *Smoothed stress field at time of failure in quasi-static simulation. Stress component S_{ij} is defined according to coordinate system in Figure 34.*

Compared to experimental tests

The flexural behavior and the gradual plastification of the end-plate and bolts are in compliance with the experimental findings discussed in Section 5.3.

A direct comparison is obtained by considering the force-displacement curves in Figure 45. The oscillation around the static solution is because of stress waves generated due to the suddenly applied motion in the explicit analysis. Increasing the total analysis time will reduce the significance of such oscillations at the cost of an increase in computing time. However, this is not a major issue because the oscillations are damped out when maximum load is reached.
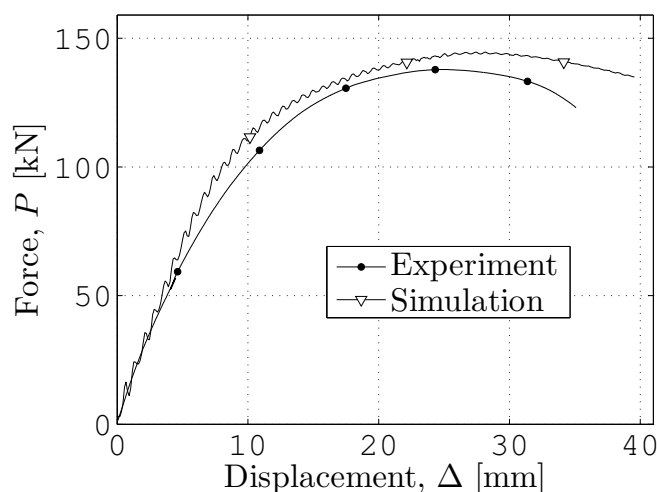

Figure 45: *Column force obtained by quasi-static simulation*

44

A stiffer response is obtained in the simulation and the model overestimates the maximum load by 4 %. The vertical displacement at failure is 15 % greater than what was measured in the experiment.

A smaller opening of the end-plate also suggests a stiffer response obtained by the finite element model as shown in Figure 46. Note that the deflection in the portal frame structure used in the experimental setup is not considered in the DIC analysis of the plate opening. Therefore, the maximum vertical displacement can not be compared to the results in Figure 45.
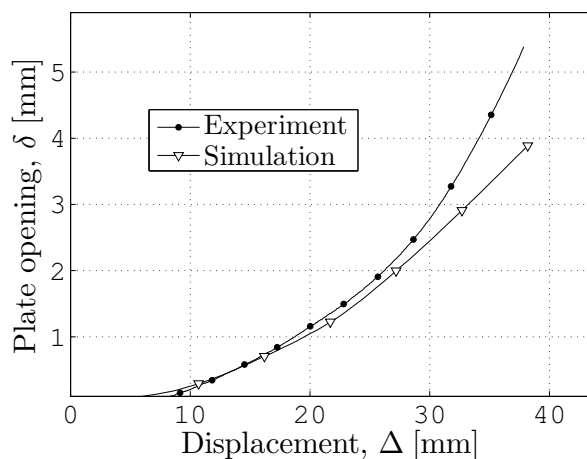

Figure 46: *Opening of the end-plate in quasi-static simulation.*

6.4 Dynamic results

Response and failure mode

The general stress state in the critical region at failure shown in Figure 47 is similar to the quasi-static simulation shown in Figure 44. A larger part of the shear force is carried by the bolts in row ③, which were not active under quasi-static loading conditions.

An approximate 8-9 % increase in the stress values is observed in the dynamic simulation. Local plastic strain rates of the order of 10 per second correspond to a 10 % increase in the yield stress in the visco-plastic material model. The viscous stress can therefore explain the slightly higher stress values.
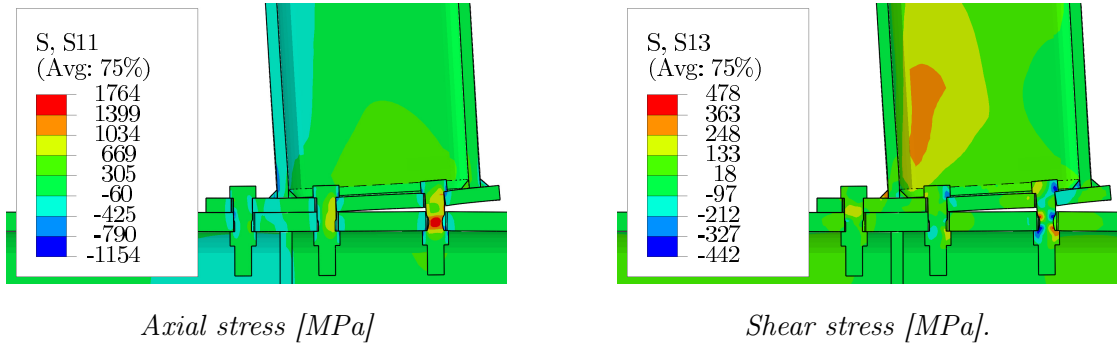
Axial stress [MPa]   Shear stress [MPa].

Figure 47: *Smoothed stress field at time of failure (9 ms after first impact). Stress component S_{ij} is defined according to coordinate system in Figure 34*

Compared to experimental tests

The simulated force measurements are compared to the experimental results in Figure 48. The peak impact force of approximately 1400 kN and the 2 ms delay until reaction forces are captured at support are in compliance with experiment. However, the response deviates over time. Two collisions were observed in the experiment, while simulation shows three hits by the trolley before failure.
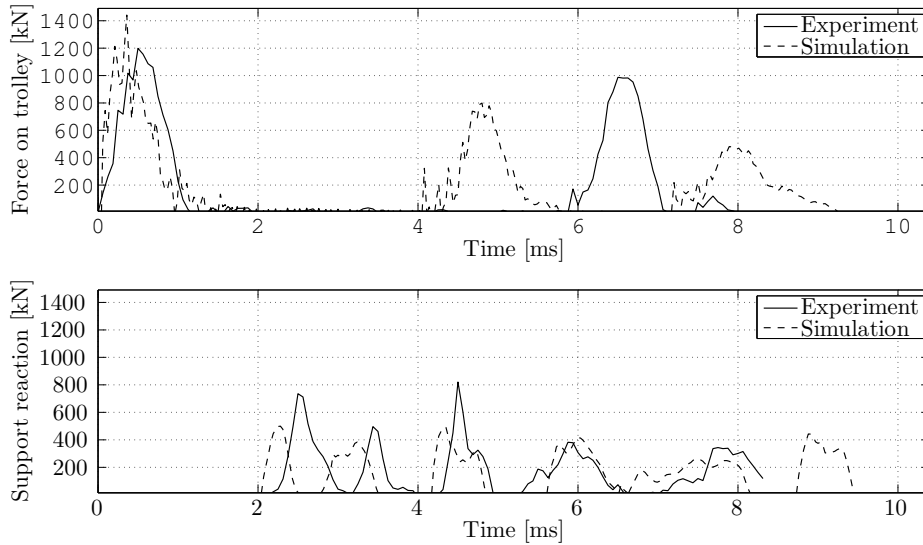

Figure 48: *Forces obtained by dynamic simulation.*

A comparison of the opening of the end-plate is shown in Figure 49. As for the quasi-static simulation, a smaller plate opening is found, further indicating an overly stiff response obtained by the finite element method.

46
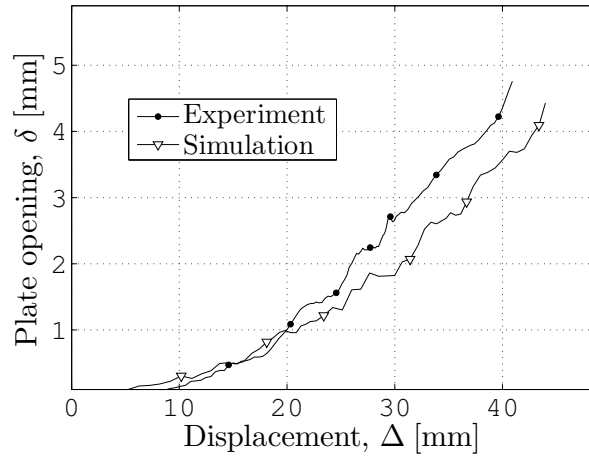
Figure 49: End-plate opening in dynamic simulation.

Response to an impulse load

It is interesting to further investigate how the connection responds to sudden dynamic forces. An exaggerated scale factor has therefore been used in Figure 50 to display the response behavior during one impact.

0.5 ms after impact   *1 ms after impact.*   *2 ms after impact.*

Figure 50: Simulated response during a sudden impact. Deformation scale factor 15.

The initial hit is causing rigid body movement of the column. All three bolt rows are therefore hit simultaneously and must transmit shear forces to inertial

resistance in the beams, which occur due to the sudden acceleration of the mass.

Shear waves require time to travel outwards to the support before reaction forces can arise. In fact, 2 ms after impact, the support is hit by the beam. The observed delay in both the simulation and the experimental test can therefore be explained.
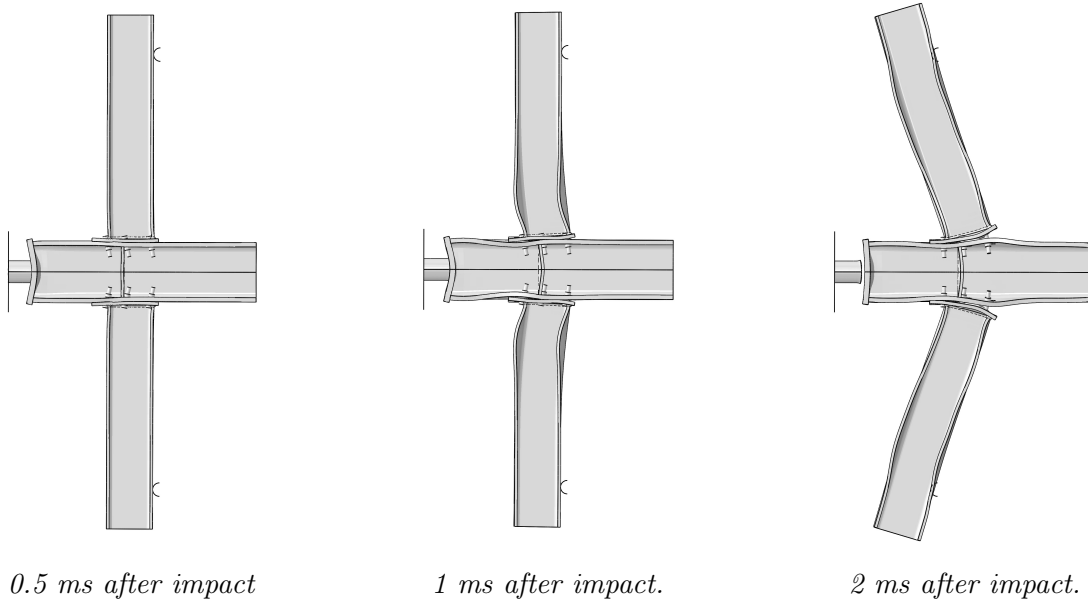
The stress state 0.5 ms after impact is pictured in Figure 51, showing the uniform distribution of shear forces to the bolts. Stress value of 396 MPa is 80 % of yield stress ($\tau_{yd} = f_y/\sqrt{3}$).
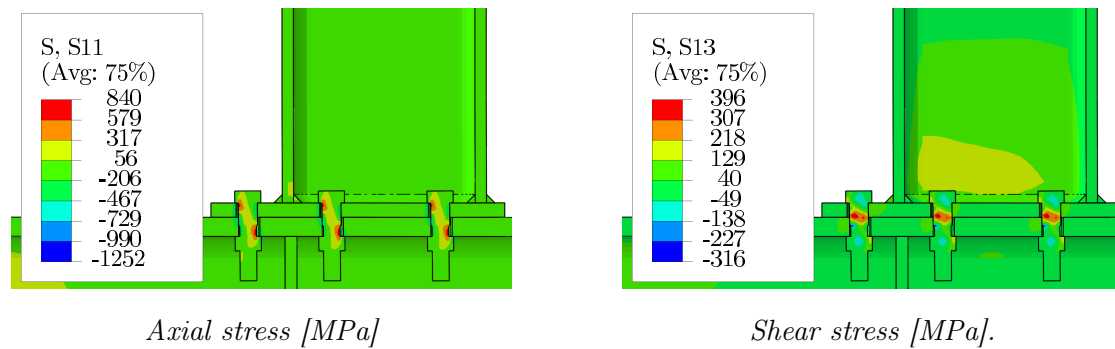

<div align="center">Axial stress [MPa]   Shear stress [MPa].</div>

Figure 51: *Smoothed stress field 0.5 ms after first impact by trolley. Stress component S_{ij} is defined according to coordinate system in Figure 34*

7 Discussion

7.1 Experimental findings

A flexural behavior of the joint due to bending was observed under both quasi-static and dynamic loading conditions. The experiments showed an initial linear response with a gradual decrease in stiffness due to plastification of the end-plate and bolts. Ultimately, the outermost bolt row failed in tension due to the excessive opening of the end-plate. After unloading, some plastic deformation was observed in the end-plate, while the column flange remained in the elastic region.

The inertial resistance that develops in the beams will undoubtedly affect the response in a dynamic load scenario. Specifically, the shear forces will have a relatively larger impact on the response compared to the bending moments as discussed in Section 1.1. However, the short impulse loads on the column in the dynamic crash test did not cause shear failure of bolts or welds, even though the peak load of 1200 kN was tenfold that of the maximum load under quasi-static conditions. Overall, the particular bolted end-plate connection investigated in the experimental program was resistant to any brittle fracture that can occur when the forces are applied suddenly.

On the other hand, the relatively small plate opening at time of failure and the absence of any plastic deformations in the beam flange suggests a poor rotational capacity. Even though this is somewhat outside the scope of this thesis, the joint would likely have performed better if a reduction in the end-plate thickness or an increase in the bolt diameter had been made. A large degree of plastic deformation is desirable and is a key feature in the development of catenary action and therefore the prevention of progressive collapse in a column removal scenario.

7.2 Assessment of the Component method (Eurocode 3)

Design rules given in current European standards have been followed to determine the strength and the stiffness of the joint. A relatively complex model is used in the Component method, where mechanical properties can be assigned individually to components such as flange, web, end-plate and bolt.

Nominal values of the material properties are typically used in design. In reality, the steel supplier is only concerned whether the minimum requirements are met, therefore delivering steel grades that often exceeds the nominal values. All the material parameters used were therefore taken from the tensile test program.

The force-displacement curve obtained is compared to the finite element simulations and the experimental results in Figure 52.
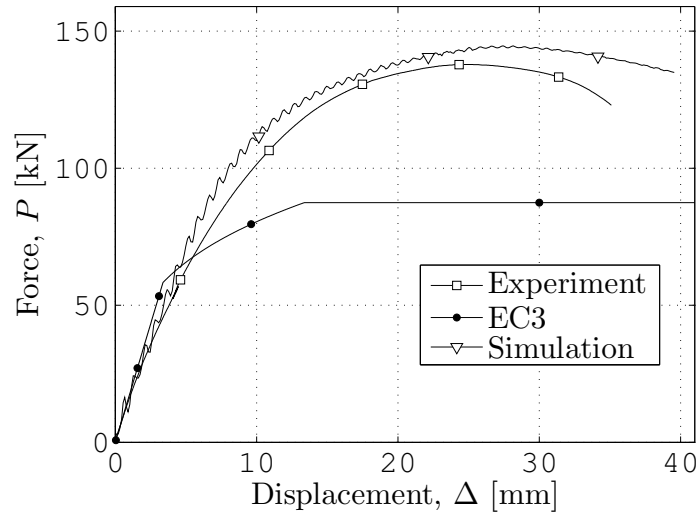
Figure 52: *A comparison of the quasi-static results.*

In despite of efforts to not make any conservative assumptions, the maximum load capacity was greatly underestimated by a factor of 1.6. In real design, load- and material coefficients would have been included, further increasing the safety. The initial stiffness was slightly overestimated. However, there are some uncertainties in the simplified stiffness model established in Figure 13.

To better understand the limitations in the Component method, a representation of the critical yield mechanism is compared to the simulated plastic strain field in Figure 53.

Figure 53: *Critical yield mechanism obtained from Component method (left) and simulated plastic strain field (right).*

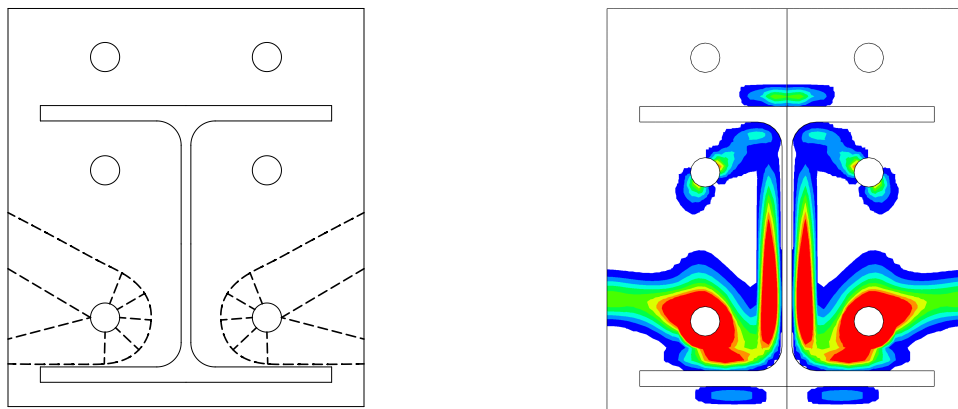Only one of the inner bolt rows (between the beam flanges) is considered in the yield mechanism. In the "normal" design case, with an extended end-plate in the tensile zone, two bolt rows are included. The performance of the joint in this particular design configuration was investigated in the paralell Master's thesis by Baasen and Nordgaard [9]. They found a significant underestimation of the capacity by a factor of 1.5 and a slightly stiffer initial response, in accordance with findings in this thesis. Therefore, the load direction is not an important factor in the Component method for this particular joint.

Another consideration is the yielding of the end-plate around the upper beam flange. The simulated strain field in Figure 53 shows an additional resistance in bending of the end-plate that is not part of the yield mechanism. This may be a contributor to the underestimation of the capacity.

It is evident that some simplifications must be made for it to be feasible to calculate by hand. Increasing the complexity of the method will not only lead to a time consuming and expensive design process, but also increase the possibility of making errors. Another important point is that the method must work in general for all types of bolted and welded connections.

Although complete calculations of the rotational capacity have not been performed, it turned out that the joint do not satisfy the basic requirements for rigid plastic global analysis, preventing the designer from utilizing the increased capacity due to catenary action (see Appendix B). This is in compliance with the experimental findings, where only limited plastic deformation was observed at time of failure. The requirements in the code can be met either by increasing the bolt diameter to 24 mm or by reducing the end-plate thickness to 8 mm.

7.3 Finite element predictions

Quasi static simulations

Finite element analyses gave a more complete understanding of the load transfer through the joint until failure. The force-displacement curve in Figure 52 reveals that the maximum load was overestimated by only 4 %, while the initial stiffness was found to be slightly greater. The opening of the end-plate during loading was underestimated, also suggesting a stiffer response obtained by finite element model.

The deviations may partially be explained by the uncertainty in the beam span. As shown in Section 6.2, an increase in the beam span of only 15 mm will reduce the maximum force by 2 % and reduce the stiffness. The experimental setup allowed for a lengthening of the distance to the support because of friction in the tests as discussed in Section 5.3. In addition, the flexibility of the portal frame structure itself may have contributed to horizontal displacement of the support.

Another possible source of error is the geometry used in the finite element

51

model. In particular, the thickness of the end-plate, which was measured to deviate as much as 1 mm from nominal thickness of 12 mm.

Simplifications in the modeling of the bolt were made, a critical component in the assembly. Thread interaction was not included, therefore preventing the observed thread stripping fracture to be simulated. However, the Cockcroft Latham criterion performed reasonably well in predicting tensile fracture of the bolts. A smaller opening of the end-plate indicates that the value of the critical strain energy used in the constitutive model (W_c) was too low. As discussed in Section 4.5, W_c will vary over the thickness in the neck region due to triaxiality and an average value was simply chosen.

Dynamic simulations

The general response characteristics were simulated in accordance with observations. A series of elastic collisions by the trolley and the ultimate flexural failure were captured by the finite element model. As for the quasi static simulations, an overly stiff response was found.

Furthermore, it was difficult to reproduce the response exactly. The additional dimension of time adds to the complexity, and small variations can lead to a very different outcome over time.
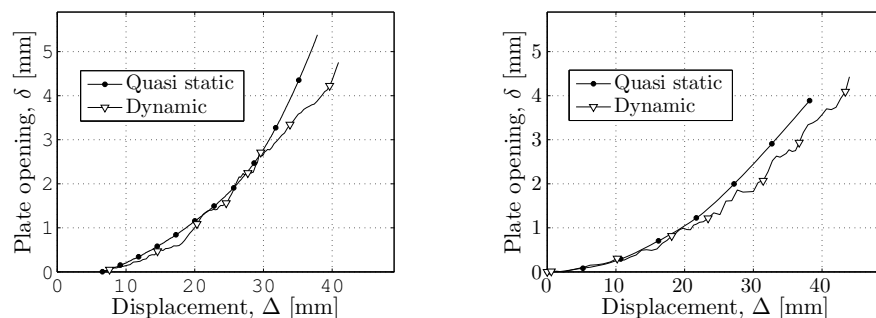

Figure 54: *Opening between end-plate and column flange at position of bolt row 1. Experiments (left) and simulations (right).*

As Figure 54 indicates, a reduction in the end-plate opening in the dynamic experiment was not predicted correctly. Contrary to the experimental findings, a larger plate opening is obtained in the dynamic simulation at time of failure. This was also found in the paralell Master's thesis by Baasen and Nordgaard [9]. As discussed in Section 6.4, the stress values are generally increased in the dynamic simulation due to viscous effects. A closer look at the stress state in bolt row ① at time of failure in Figure 55 further support this finding. The maximum principal stress (used in Cockroft and Latham fracture criterion) is increased by

approximately 12 % in the dynamic simulation. Therefore, one would expect the strain energy in Eq. (7) to increase by the same factor and hence reducing the plate opening at time of failure. Unfortunately, the cause of this unexpected result has not been found.
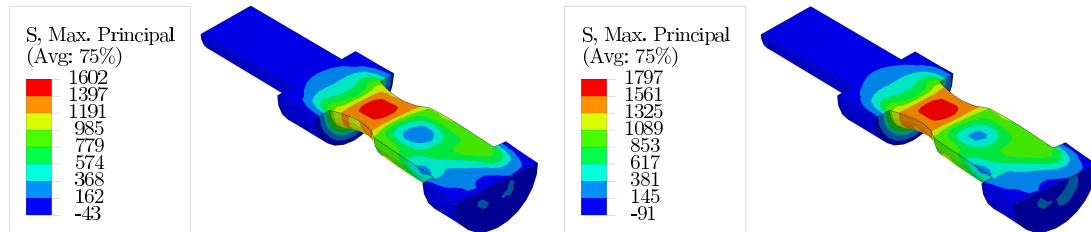

Figure 55: *Maximum principal stress [MPa] in bolt row 1 at time of failure. Quasi-static simulation (left) and dynamic simulation (right).*

The change in the response characteristics due to inertial resistance in a dynamic impact was investigated in Section 6.4. The simulation revealed that very high shear stress develops at the time of impact, and all three bolt rows are active in the load transfer.

Additional simulations have been conducted to try to impose the expected change from flexural to shear failure. An increase in the velocity of the trolley from 6 m/s to 20 m/s did not cause shear failure of bolts or welds. A possible explanation is that tensile separation is the underlying concept of the Cockcroft and Latham fracture criterion used in the finite element model.

8 Conclusions and suggestions for further work

8.1 Concluding remarks

1. Vertical displacement of the column lead to failure in flexure as predicted by Eurocode and the finite element models.

2. Thread stripping fracture was observed in one of the experiments, but was not captured by any of the design methods.

3. As expected, the simplified methods given in design codes gave safe estimates of the capacity, while numerical simulations allowed for a more accurate description of the response characteristics and failure mode.

4. As previous research has shown, the initial stiffness was overestimated by both Eurocode's method and the finite element models.

5. The Component method in Eurocode 3 showed no limitations in predicting the quasi-static response when the force direction was reversed. However, an overly safe estimate of the capacity was obtained.

6. The numerical simulations revealed that the relative impact of shear forces is increased when the column is subjected to rapid, non cyclic loading.

8.2 Future studies

Possible subjects for further work:

- Further investigations into what load scenario will cause the expected change from flexural to shear failure when forces are applied suddenly. The introduction of an additional failure criterion based on shear glide should be implemented in the finite element model.

- Parametric study: Investigate the effect of catenary action in a structural collapse scenario by numerical simulations.

- Parametric study: Optimization of bolted end-plate connections. Can include placement of bolts, thickness of end-plate, extended vs flush etc.

References

[1] European Committee for Standardization (CEN). Eurocode - 1990 - basis of structural design, February 2008.

[2] A. Coelho, F. Bijlaard, and L. da Silva. Experimental assessment of the ductility of extended end plate connections. *Engineering Structures*, 26:1185–1206, 2004.

[3] European Committee for Standardization (CEN). Eurocode - 1993 - design of steel structures - part 1-8: Design of joints, May 2005.

[4] B. Yang and K. H. Tan. Numerical analyses of steel beam-column joints subjected to catenary action. *Journal of Constructional Steel Research*, 70: 1–11, 2011.

[5] B. Yang and K. H. Tan. Experimental test of different types of bolted steel beam-column joints under a central-column-removal scenario. *Engineering Structures*, 54:112–130, 2013.

[6] F.H. Sadek, H. S. Lew, J. Main, S.D Robert, and V. P. Chiarito. Performance of steel moment connections under a column removal scenario. i: Experiments. *Journal of Structural Engineering*, 139:98–107, 2013.

[7] F. Sadek, J. Main, H. Lew, and S. El-Tawil. Performance of steel moment connections under a column removal scenario. ii: Analysis. *Journal of Structural Engineering*, 139:108–119, 2013.

[8] T Subawala, D Linzell, and T Krauthammer. Finite element analysis of steel beam to column connections subjected to blast loads. *International Journal of Impact Engineering*, 31:861–876, 2004.

[9] Gjermund Baasen and Torger Nordgaard. Beam-column connections subjected to static and dynamic loading. Master's thesis, Norwegian University of Science and Technology (NTNU), 2014.

[10] P. K. Larsen. *Dimensjonering av staalkonstruksjoner (Design of steel structures)*. Tapir Akademiske Forlag, 2010.

[11] O.S. Hopperstad and T. Boervik. Lecture notes, TKT4135 Materials Mechanics. Norwegian University of Science and Technology (NTNU), spring 2013.

[12] F. Irgens. *Continuum Mechanics*. Tapir Akademiske Forlag, 2008.

[13] J. Lubliner. *Plasticity Theory.* Macmillan Pub Co, 1998.

[14] J. Lemaitre and J.-L. Chaboche. *Mechanics of Solid Materials.* Cambridge University Press, 1994.

[15] M. G. Cockcroft and D. J. Latham. Ductility and the workability of metals. *Journal of the Institute of Metals*, 96:33–39, 1968.

[16] K.E. Yazzie, H. Fei, H. Jiang, and N. Chawla. A self-consistent approach for necking correction intensile specimens with rectangular cross-section using a novel mirror fixture. *Transactions A: Physical Metallurgy and Materials Science*, 43A:5058–5066, 2012.

[17] P. W. Bridgman. *Studies in Large Plastic Flow and Fracture.* McGraw-Hill, 1952.

[18] M. A. Sutton, S. R. McNeill, J. D. Helm, and Y. J. Chao. Advances in two-dimensional and three-dimensional computer vision. *Topics in Applied Physics*, 77:323–372, 2000.

[19] M. A. Sutton, M. Cheng, W. H. Peters, and Y. J. Chao. Application of an optimized digital correlation method to planar deformation analysis. *Image and Vision Computing*, 4:143–150, 1986.

[20] Y. Chen, A. H. Clausen, O.S. Hopperstad, and M. Langseth. Application of a split-hopkinson tension bar in a mutual assessment of experimental tests and numerical predictions. *International Journal of Impact Engineering*, 38: 824–836, 2011.

[21] E Fagerholt. ecorr v3.0 digital image correlation tool by simlab. NTNU, 2013.

[22] H.A. Khoo, M. Cheng, and T.M. Hrudey. Determine steel properties for large strain from a standard tension test. In *2nd Material Specialty Conference of the Canadian Society for Civil Engineering*, 2002.

[23] A. G. Hanssen, T. Auestad, T. Tryland, and M. Langseth. The kicking machine: A device for impact testing of structural components. *International Journal of Crashworthiness*, 8:385–392, 2003.

[24] *Abaqus 6.12 User Documentation.* Dassault Systemes, February 2012.

[25] SIMLab. *Theory Manual: SIMLab Metal Model.* Norwegian University of Science and Technology (NTNU), 2014.

[26] *Abaqus 6.12 Theory Manual.* Dassault Systemes, February 2012.

[27] European Committee for Standardization (CEN). Eurocode - 1993 - design of steel structures - part 1-1: General rules and rules for buildings, May 2005.

[28] European Committee for Standardization (CEN). Execution of steel structures and aluminium structures - part 1: Requirements for conformity assessment of structural components, May 2012.

[29] European Committee for Standardization (CEN). High-strength structural bolting assemblies for preloading - part 7: System hr - countersunk head bolt and nut assemblies, May 2007.

A   Capacity according to NS EN 1993-1-8

Two beams (HEA 180) are connected to a column (HEB 220) using an end-plate and 6 bolts (M16).
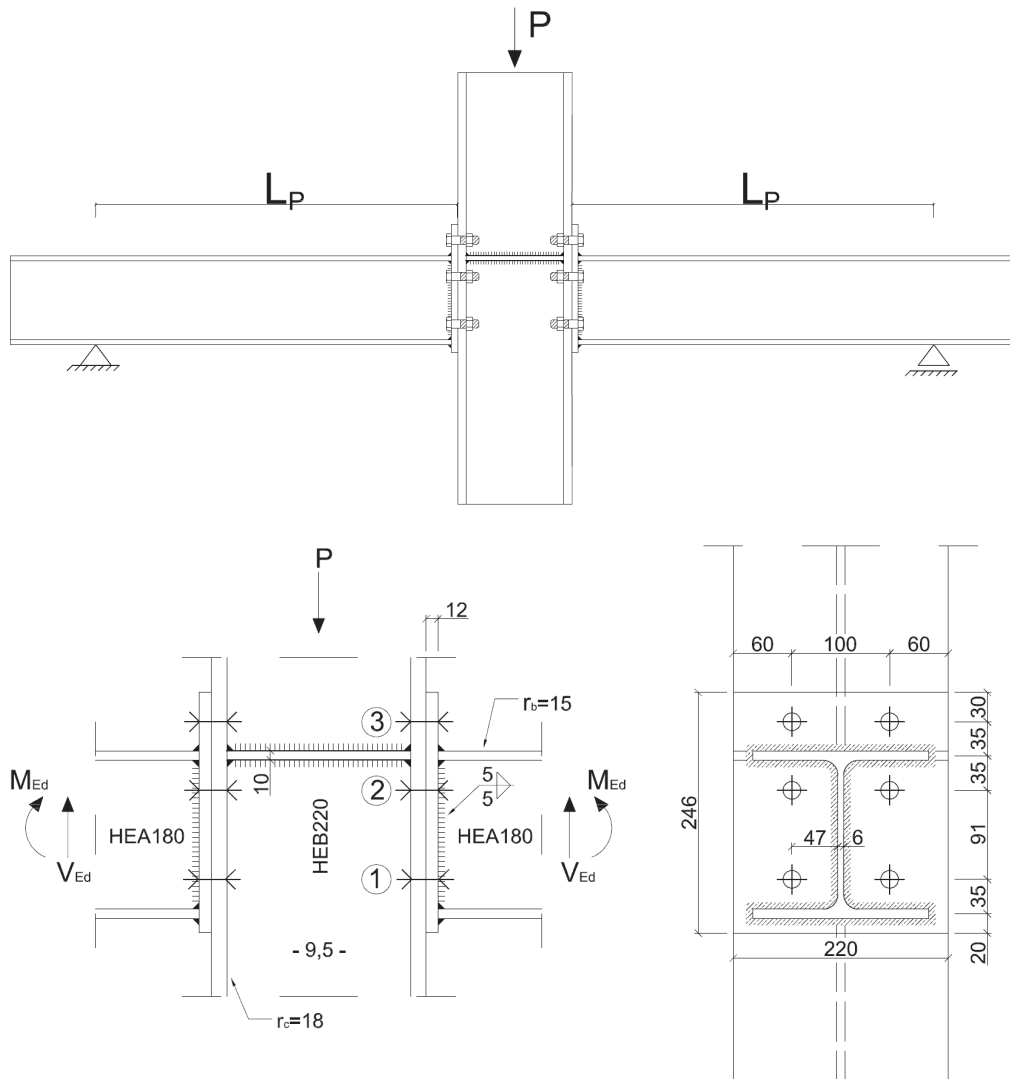
The capacity of the joint is checked for a point load P = 87 kN.

Point load:

$P := 87.2 \text{kN}$

$L_P := 697 \text{mm}$

Partial factors:

$\gamma_{M0} := 1.0$

$\gamma_{M1} := 1.0$

$\gamma_{M2} := 1.0$

Elastic modulus:

$E_S := 210000 \text{MPa}$

1. INPUT DATA

Beam data (HEA 180)

$f_{y.b} := 442\,MPa$

$b_b := 180\,mm$

$h_b := 171\,mm$

$t_{f.b} := 9.5\,mm$

$t_{w.b} := 6\,mm$

$r_b := 15\,mm$

$A_b := 4.53 \cdot 10^3\,mm^2$

$S_{y.b} := 162 \cdot 10^3\,mm^3$

$f_{u.b} := 554\,MPa$

(rolled section) $s_b := r_b = 15 \cdot mm$

Column data (HEB 220)

$f_{y.c} := 400\,MPa$

$b_c := 220\,mm$

$h_c := 220\,mm$

$t_{f.c} := 16\,mm$

$t_{w.c} := 9.5\,mm$

$r_c := 18\,mm$

$A_c := 9.10 \cdot 10^3\,mm^2$

$S_{y.c} := 414 \cdot 10^3\,mm^3$

$f_{u.c} := 539\,MPa$

$s_c := r_c = 18 \cdot mm$

Bolts

$d := 16\,mm$ (bolt class 8.8)

$d_0 := 18\,mm$

$k_2 := 0.9$

$\alpha_v := 0.6$ (full threaded)

$f_{ub} := 946\,MPa$

$f_{yb} := 865\,MPa$

$A_s := 157\,mm^2$

$h_{b.n} := 12\,mm$ (heigth of nut)

$h_{b.h} := 10\,mm$ (heigth of head)

End plate

$t_p := 12\,mm$

$b_p := 220\,mm$

$f_u := 562\,MPa$

$f_y := 412\,MPa$

$e_1 := 30\,mm$

$e_2 := 60\,mm$

$p_1 := 70\,mm$

$p_2 := 100\,mm$

$e_5 := 35\,mm$ (from row 1 to upper flange)

$p_5 := 91\,mm$ (from row 1 to row 2)

Welds

$a_f := 5\,mm$

$a_w := 5\,mm$

$\beta_w := 0.9$

2. BOLT DESIGN

Figure 6.15(c)

Centre of compression in line with mid-thickness of the compression flange.

Bolt row 2 is located close to centre of compression and is neglected in all calculations. Thus bolt row 1 are the only bolts active in tension.

Bolt row 3 is designed to take shear force V_{Ed}.

SHEAR FORCE CHECK

Design shear force:

$$V_{Ed} := \frac{P}{2} = 43.6 \cdot kN$$

Shear resistance:

$$F_{v.Rd} := \frac{\alpha_v \cdot f_{ub} \cdot A_s}{\gamma_{M2}} = 89 \cdot kN \qquad \text{(per bolt)}$$

For bolt row 3:

$$F_{v.Rd'} := 2 \cdot F_{v.Rd} = 178 \cdot kN$$

Bearing resistance:

Flange beween bolt row 3 and bolt row 2 prevents shear tearing between bolts in end plate. Local failure mode assumed.

$$k_1 := 2.5$$

$$\alpha_b := \min\left(\frac{f_{ub}}{f_u}, 1\right) = 1$$

$$t := \min\left(t_{f.c}, t_p\right) = 12 \cdot mm$$

$$F_{b.Rd} := \frac{k_1 \cdot \alpha_b \cdot f_u \cdot d \cdot t}{\gamma_{M2}} = 270 \cdot kN \qquad \text{(per bolt)}$$

For bolt row 3:

$$F_{b.Rd'} := 2 \cdot F_{b.Rd} = 540 \cdot kN$$

Shear capacity for bolt row 3:

$$F_{Rd} := min(F_{v.Rd'}, F_{b.Rd'}) = 178 \cdot kN$$

$$Shear_{bolt.req} := \begin{vmatrix} "OK" & if \ F_{Rd} \geq V_{Ed} \\ "NOT \ OK" & otherwise \end{vmatrix} = "OK"$$

TENSION CHECK

Figure 6.15(c):

The moment, M_{Ed}, is carried by flange force, N_f. Lever arm, z, is the distance between the compression flange to bolts in tension (row 1).

$$z := e_5 + p_5 = 126 \cdot mm$$

5.3 (2) and (4)

The connection elements should be designed for the forces at the periphery of the column web panel.

$$M_{Ed} := \frac{P}{2} \cdot (L_P + t_{f.c}) = 31.1 \cdot kN \cdot m$$

$$N_{f.Ed} := \frac{M_{Ed}}{z} = 247 \cdot kN$$

Tension capacity:

$$F_{t.Rd} := \frac{k_2 \cdot f_{ub} \cdot A_s}{\gamma_{M2}} = 134 \cdot kN \qquad\qquad (per \ bolt)$$

Tension capacity for bolt row 1:

$$F_{t.Rd'} := 2 \cdot F_{t.Rd} = 267 \cdot kN$$

$$Tension_{bolt.req} := \begin{vmatrix} "OK" & if \ F_{t.Rd'} \geq N_{f.Ed} \\ "NOT \ OK" & otherwise \end{vmatrix} = "OK"$$

3. TENSION FLANGE CHECK

$$A_f := b_b \cdot t_{f.b} = 1.71 \times 10^3 \cdot mm^2$$

$$f_d := \frac{f_{y.b}}{\gamma_{M0}} = 442 \cdot MPa$$

Yield capacity of beam flange:

$$N_{fb.Rd} := A_f \cdot f_d = 756 \cdot kN$$

$$Tension_{flange.req} := \begin{vmatrix} "OK" & if \ N_{fb.Rd} \geq N_{f.Ed} \\ "NOT \ OK" & otherwise \end{vmatrix} = "OK"$$

4. COMPRESSION FLANGE CHECK

6.2.6.7

Yield capacity of compressed flange is at least the same as for tension flange.

See formula 6.21

5. CAPACITY OF WELDS

FLANGE WELD

Given, $a_f = 5 \cdot mm$

Design throat area:

4.5.3.2.(2)

$l_{eff.f} := b_b + 2 \cdot t_{f.b} + \left(b_b - 2 \cdot r_b - t_{w.b}\right) = 343 \cdot mm$

$A_{w.f} := a_f \cdot l_{eff.f} = 1.715 \times 10^3 \cdot mm^2$

Design tension strength of the weld:

4.5.3.2.(6)

$f_{vw.fb.d} := \dfrac{f_{u.b}}{\sqrt{2} \cdot \gamma_{M2} \cdot \beta_w} = 435 \cdot MPa$

<u>Design resistance of flange weld in tension:</u>

$F_{w.fb.Rd} := A_{w.f} \cdot f_{vw.fb.d} = 746 \cdot kN$

$Tension_{weld.req} := \begin{array}{|l} \text{"OK"} \quad \text{if } F_{w.fb.Rd} \geq N_{f.Ed} \quad = \text{"OK"} \\ \text{"NOT OK"} \quad \text{otherwise} \end{array}$

WEB WELD

Given, $a_f = 5 \cdot mm$

Design throat area:

4.5.3.2.(2)

$l_{eff.w} := \left(h_b - 2 \cdot t_{f.b} - 2 \cdot r_b\right) \cdot 2 = 244 \cdot mm$

$A_{w.w} := a_f \cdot l_{eff.w} = 1.22 \times 10^3 \cdot mm^2$

4.5.3.2.(6)

and

4.5.3.3.(3)

Design shear strength of the weld:

$f_{vw.wb.d} := \dfrac{f_{u.b}}{\sqrt{3} \cdot \gamma_{M2} \cdot \beta_w} = 355 \cdot MPa$

Design resistance of web weld in shear:

$$F_{w.wb.Rd} := A_{w.w} \cdot f_{vw.wb.d} = 434 \cdot kN$$

$$Shear_{weld.req} := \begin{vmatrix} \text{"OK"} & \text{if } F_{w.wb.Rd} \geq V_{Ed} & = \text{"OK"} \\ \text{"NOT OK"} & \text{otherwise} \end{vmatrix}$$

6. CAPACITY OF COLUMN FLANGE IN BENDING

Bending capacity according to 6.2.6.4. An equivavalen T-stub model with an effective length, l_{eff}, is used.

Geometry:

Figure 6.8

$$m' := \frac{p_2}{2} - \frac{t_{w.c}}{2} - 0.8 \cdot r_c = 31 \cdot mm$$

$$e_{min} := e_2 = 60 \cdot mm$$

$$e' := e_{min} = 60 \cdot mm$$

Effective lengths for circular (cp) and non-circular (nc) patterns:

$$l_{eff.cp.fc} := 2 \cdot \pi \cdot m' = 194 \cdot mm$$

Table 6.4

$$l_{eff.nc.fc} := 4 \cdot m' + 1.25 \cdot e' = 198 \cdot mm$$

Design resistance of T-stub representing the column flange:

$$n'' := \begin{vmatrix} e_{min} & \text{if } e_{min} < 1.25 \cdot m' & = 39 \cdot mm \\ (1.25 \cdot m') & \text{otherwise} \end{vmatrix}$$

Failure mode 1 (complete yielding of plate)

$$l_{eff.1.fc} := \min(l_{eff.cp.fc}, l_{eff.nc.fc}) = 194 \cdot mm$$

$$M_{pl.1.fc.Rd} := 0.25 \cdot l_{eff.1.fc} \cdot t_{f.c}^2 \cdot \frac{f_y}{\gamma_{M0}} = 5.111 \cdot kN \cdot m$$

$$F_{T.1.fc.Rd} := \frac{4 \cdot M_{pl.1.fc.Rd}}{m'} = 663 \cdot kN$$

Failure mode 2 (bolt failure and yielding of plate)

$$l_{eff.2.fc} := l_{eff.nc.fc} = 198 \cdot mm$$

$$M_{pl.2.fc.Rd} := 0.25 \cdot l_{eff.2.fc} \cdot t_{f.c}^2 \cdot \frac{f_y}{\gamma_{M0}} = 5.23 \cdot kN \cdot m$$

$$F_{T.2.fc.Rd} := \frac{2 \cdot M_{pl.2.fc.Rd} + n'' \cdot 2F_{t.Rd}}{m' + n''} = 299 \cdot kN$$

Failure mode 3
(bolt failure)

$$F_{T.3.fc.Rd} := 2 \cdot F_{t.Rd} = 267 \cdot kN$$

Design resistance of column flange in bending:

$$F_{T.fc.Rd} := min\left(F_{T.1.fc.Rd}, F_{T.2.fc.Rd}, F_{T.3.fc.Rd}\right) = 267 \cdot kN$$

7. CAPACITY OF END-PLATE IN BENDING

Bending capacity according to 6.2.6.5. An equivavalen T-stub model with an effective length, l_{eff}, is used.

Geometry:

Figure 6.11

$$m'' := \frac{p_2}{2} - \frac{t_{w.b}}{2} - 0.8 \cdot a_w \cdot \sqrt{2} = 41 \cdot mm$$

$$e_{min} = 60 \cdot mm$$

$$e' = 60 \cdot mm$$

$$m_2 := e_5 - \frac{t_{f.b}}{2} - 0.8 \cdot a_w \cdot \sqrt{2} = 25 \cdot mm$$

Effective lengths for circular (cp) and non-circular (nc) patterns:

Table 6.6

$$l_{eff.cp.ep} := 2 \cdot \pi \cdot m'' = 260 \cdot mm$$

$$\lambda_1 := \frac{m''}{m'' + e'} = 0.41$$

$$\lambda_2 := \frac{m_2}{m'' + e'} = 0.24$$

NOTE: "alpha" coefficient read manually from figure 6.11.

$$\alpha := 7.5$$

$$l_{eff.nc.ep} := \alpha \cdot m'' = 310 \cdot mm$$

Design resistance of T-stub representing the end-plate:

$$n''' := \begin{vmatrix} e_{min} & \text{if } e_{min} < 1.25 \cdot m'' & = 52 \cdot mm \\ (1.25 \cdot m'') & \text{otherwise} \end{vmatrix}$$

Failure mode 1
(complete yielding of plate)

$$l_{eff.1.ep} := min\left(l_{eff.cp.ep}, l_{eff.nc.ep}\right) = 260 \cdot mm$$

$$M_{pl.1.ep.Rd} := 0.25 \cdot l_{eff.1.ep} \cdot t_p^2 \cdot \frac{f_y}{\gamma_{M0}} = 3.85 \cdot kN \cdot m$$

$$F_{T.1.ep.Rd} := \frac{4 \cdot M_{pl.1.ep.Rd}}{m''} = 373 \cdot kN$$

Failure mode 2
(bolt failure and
yielding of plate)

$$l_{eff.2.ep} := l_{eff.nc.ep} = 310 \cdot mm$$

$$M_{pl.2.ep.Rd} := 0.25 \cdot l_{eff.2.ep} \cdot t_p^2 \cdot \frac{f_y}{\gamma_{M0}} = 4.6 \cdot kN \cdot m$$

$$F_{T.2.ep.Rd} := \frac{2 \cdot M_{pl.2.ep.Rd} + n''' \cdot 2 F_{t.Rd}}{m'' + n'''} = 247 \cdot kN$$

Failure mode 3
(bolt failure)

$$F_{T.3.ep.Rd} := 2 \cdot F_{t.Rd} = 267 \cdot kN$$

Design resistance of end-plate in bending:

$$\boxed{F_{T.ep.Rd} := \min\left(F_{T.1.ep.Rd}, F_{T.2.ep.Rd}, F_{T.3.ep.Rd}\right) = 247 \cdot kN}$$

8. CAPACITY OF THE COLUMN WEB IN TENSION

6.2.6.3.(3)

$b_{eff.t.wc}$ is taken as the effective length of equivalent T-stub representing the failure mechanism for column flange in bending.

$$b_{eff.t.wc} := l_{eff.1.fc} = 194 \cdot mm$$

Symmetry in loading ($M_{b1,Ed}=M_{b2,Ed}$):

$$\beta := 0$$

Table 5.4

$$\omega := 1$$

Design resistance of column web in transverse tension:

$$\boxed{F_{t.wc.Rd} := \frac{\omega \cdot b_{eff.t.wc} \cdot t_{w.c} \cdot f_{y.c}}{\gamma_{M0}} = 737 \cdot kN}$$

9. CAPACITY OF THE COLUMN WEB IN COMPRESSION

Stiffener between column flanges in compression prevents local buckling and resistance is at least the same as for web in tension.

10. CAPACITY OF THE BEAM WEB IN TENSION

6.2.6.8.(2)

$b_{eff.t.wb}$ is taken as the effective length of equivalent T-stub

representing the failure mechanism for end-plate in bending.

$$b_{eff.t.wb} := l_{eff.1.ep} = 260 \cdot mm$$

Design resistance of beam web in tension:

$$F_{t.wb.Rd} := \frac{b_{eff.t.wb} \cdot t_{w.b} \cdot f_{y.b}}{\gamma_{M0}} = 689 \cdot kN$$

11. CAPACITY OF BEAM FLANGE AND WEB IN COMPRESSION

Plastic moment resistance:

$$W_{pl.b} := 2 \cdot S_{y.b} = 3.24 \times 10^5 \cdot mm^3$$

$$M_{pl.b.Rd} := f_{y.b} \cdot W_{pl.b} = 143.2 \cdot kN \cdot m$$

Design resistance of beam flange and web in compression:

6.2.6.7

$$F_{c.fb.Rd} := \frac{M_{pl.b.Rd}}{h_b - t_{f.b}} = 887 \cdot kN$$

12. SUMMARY

Dimensioning forces $P = 87.2 \cdot kN$ $V_{Ed} = 43.6 \cdot kN$ $M_{Ed} = 31.1 \cdot kN \cdot m$ $N_{f.Ed} = 247 \cdot kN$

Shear capacities

$F_{v.Rd'} = 178 \cdot kN$ (Shear, bolt row 3) $\dfrac{V_{Ed}}{F_{v.Rd'}} = 0.24$

$F_{w.wb.Rd} = 434 \cdot kN$ (Shear, web weld) $\dfrac{V_{Ed}}{F_{w.wb.Rd}} = 0.1$

$F_{b.Rd'} = 540 \cdot kN$ (Bearing, end-plate) $\dfrac{V_{Ed}}{F_{b.Rd'}} = 0.08$

Tension/Compression capacities

$F_{t.Rd'} = 267 \cdot kN$ (Tension capacity without prying effect, bolt row 1) $\dfrac{N_{f.Ed}}{F_{t.Rd'}} = 0.92$

$F_{t.wb.Rd} = 689 \cdot kN$ (Beam web in tension) $\dfrac{N_{f.Ed}}{F_{t.wb.Rd}} = 0.36$

$N_{fb.Rd} = 756 \cdot kN$ (Yield capacity of beam flange) $\dfrac{N_{f.Ed}}{N_{fb.Rd}} = 0.33$

$F_{w.fb.Rd} = 746 \cdot kN$ (Flange weld in tension) $\dfrac{N_{f.Ed}}{F_{w.fb.Rd}} = 0.33$

$F_{c.fb.Rd} = 887 \cdot kN$ (Beam flange and web in compression) $\dfrac{N_{f.Ed}}{F_{c.fb.Rd}} = 0.28$

Capacity of end-plate in bending due to tension

$F_{T.2.ep.Rd} = 247 \cdot kN$ (Bolt failure and yielding of end-plate) $\dfrac{N_{f.Ed}}{F_{T.2.ep.Rd}} = 1.00$

$F_{T.3.ep.Rd} = 267 \cdot kN$ (Bolt failure) $\dfrac{N_{f.Ed}}{F_{T.3.ep.Rd}} = 0.92$

$F_{T.1.ep.Rd} = 373 \cdot kN$ (Complete yielding of end-plate) $\dfrac{N_{f.Ed}}{F_{T.1.ep.Rd}} = 0.66$

Capacity of column flange in bending due to tension

$F_{T.3.fc.Rd} = 267 \cdot kN$ (Bolt failure) $\dfrac{N_{f.Ed}}{F_{T.3.fc.Rd}} = 0.92$

$F_{T.2.fc.Rd} = 299 \cdot kN$ (Bolt failure and yielding of flange) $\dfrac{N_{f.Ed}}{F_{T.2.fc.Rd}} = 0.82$

$F_{T.1.fc.Rd} = 663 \cdot kN$ (Complete yielding of flange) $\dfrac{N_{f.Ed}}{F_{T.1.fc.Rd}} = 0.37$

Capacity of column web

$F_{t.wc.Rd} = 737 \cdot kN$ (Column web in tension) $\dfrac{N_{f.Ed}}{F_{t.wc.Rd}} = 0.33$

Design moment resistance of joint

(one bolt-row active in tension) $h_1 := z = 126 \cdot mm$

(bolt failure and yielding of end-plate) $F_{t1.Rd} := \min\left(F_{T.fc.Rd}, F_{T.ep.Rd}\right) = 247 \cdot kN$

Design moment resistance:

6.2.7.2.(1) $M_{j.Rd} := h_1 \cdot F_{t1.Rd} = 31.2 \cdot kN \cdot m$

B Stiffness according to NS EN 1993-1-8

Two beams (HEA 180) are connected to a column (HEB 220) using an end-plate and 6 bolts (M16). The stiffness properties of the joint are represented by a set of linear springs. One side of the double sided joint are depicted below.
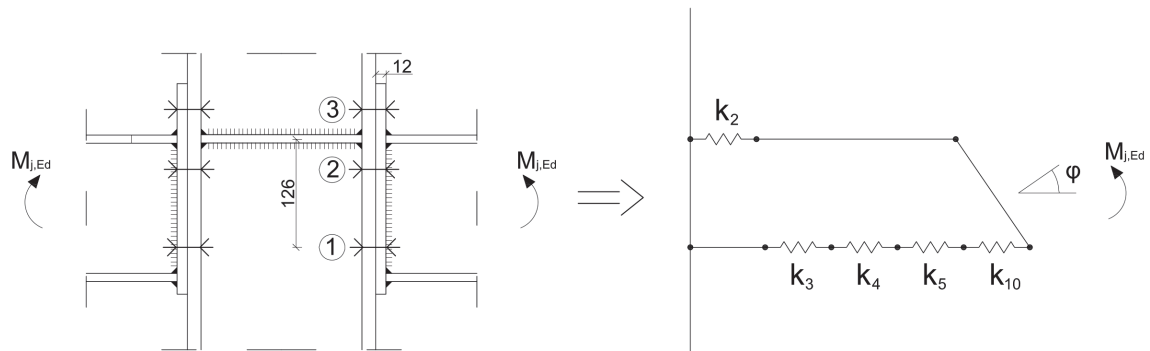
The rotational stiffness of the joint is established and the rotation capacity is checked.

1. ELASTIC STIFFNESS COEFFICIENTS

Table 6.10

For two sided bolted joints with equal and opposite moments, the components to be taken into account are:

- k_2 column web in compression
- k_3 column web in tension
- k_4 column flange in bending
- k_5 end-plate in bending
- k_{10} bolts in tension

COLUMN WEB IN COMPRESSION

Table 6.11

The stiffness contribution for a stiffened column web is neglected:

$$k_2 = \infty$$

COLUMN WEB IN TENSION

Table 6.11

$b_{eff.t.wc}$ is the effective width of column web in tension, and is taken as the effective length of equivalent T-stub representing the failure mechanism for column flange in bending.

6.2.6.3.(3)

$$b_{eff.t.wc} = 194 \cdot mm$$

Shear length, column web:

$$d_{cw} := h_c - 2 \cdot t_{f.c} - 2 \cdot r_c = 152 \cdot mm$$

Column web thickness:

$$t_{w.c} = 9.5 \cdot mm$$

Stiffness coefficient for column web in tension:

$$k_3 := \frac{0.7 \cdot b_{eff.t.wc} \cdot t_{w.c}}{d_{cw}} = 8.5 \cdot mm$$

COLUMN FLANGE IN BENDING

Table 6.11

l_{eff} is to be taken as the smallest effective length used in equivavelent T-stub representing the column flange in bending.

Table 6.4

$$l_{eff.4} := min\left(l_{eff.cp.fc}, l_{eff.nc.fc}\right) = 194 \cdot mm$$

Figure 6.8

$$m' = 31 \cdot mm$$

Stiffness coefficient for column flange in bending:

$$k_4 := \frac{0.9 \cdot l_{eff.4} \cdot t_{f.c}^3}{m'^3} = 24.3 \cdot mm$$

END-PLATE IN BENDING

Table 6.11

l_{eff} is to be taken as the smallest effective lengths used in equivavelent T-stub representing the end-plate in bending.

Table 6.6

$$l_{eff.5} := min\left(l_{eff.cp.ep}, l_{eff.nc.ep}\right) = 260 \cdot mm$$

Figure 6.11

$$m'' = 41 \cdot mm$$

Stiffness coefficient for end-plate in bending:

$$k_5 := \frac{0.9 \cdot l_{eff.5} \cdot t_p^3}{m''^3} = 5.7 \cdot mm$$

BOLTS IN TENSION

Only one bolt-row considered active in tension (row 1).

Table 6.11

L_b taken as the bolt elongation length, taken as the grip thickness (material and washers), plus half the heigth of bolt head and nut. Washers are not used in connection.

$$L_b := t_{f.c} + t_p + \frac{h_{b.h}}{2} + \frac{h_{b.n}}{2} = 39 \cdot mm$$

Stress area, bolt:

$$A_s = 157 \cdot mm^2$$

Stiffness coefficient for bolts in tension:

$$k_{10} := 1.6 \cdot \frac{A_s}{L_b} = 6.4 \cdot mm$$

2. ROTATIONAL STIFFNESS

EQUIVALENT STIFFNESS IN TENSION

For case with only one bolt row in tension:

6.3.3.1.(1)

$$k_{eq} := \frac{1}{\dfrac{1}{k_3} + \dfrac{1}{k_4} + \dfrac{1}{k_5} + \dfrac{1}{k_{10}}} = 2.044 \cdot mm$$

INITIAL ROTATIONAL STIFFNESS

Lever arm:

$$z = 126 \cdot mm$$

Initial rotational stiffness:

6.3.1.(4)

$$S_{j.ini} := \frac{E_s \cdot z^2}{\dfrac{1}{k_{eq}}} = 6.82 \times 10^3 \cdot kN \cdot \frac{m}{rad}$$

ROTATIONAL STIFFNESS

Design moment:

$$M_{j.Ed} := 0, 0.01kN \cdot m \, .. \, 60kN \cdot m$$

Coefficient for bolted end-plate:

Table 6.8 $\qquad \psi := 2.7$

Stiffness ratio:

6.3.1.(6) $\qquad \mu\left(M_{j.Ed}\right) := \begin{array}{|l} 1.0 \quad \text{if } M_{j.Ed} \le \dfrac{2}{3} M_{j.Rd} \\[2em] \left(1.5 \cdot \dfrac{M_{j.Ed}}{M_{j.Rd}}\right)^{\psi} \quad \text{if } \dfrac{2}{3} \cdot M_{j.Rd} < M_{j.Ed} \le M_{j.Rd} \end{array}$

Rotational stiffness:

6.3.1.(4) $\qquad S_j\left(M_{j.Ed}\right) := \dfrac{E_s \cdot z^2}{\mu\left(M_{j.Ed}\right) \cdot \dfrac{1}{k_{eq}}}$

Rotation (rad):

$\phi\left(M_{j.Ed}\right) := \begin{array}{|l} \dfrac{M_{j.Ed}}{S_j\left(M_{j.Ed}\right)} \quad \text{if } M_{j.Ed} \le M_{j.Rd} \\[1.5em] 100 \quad \text{otherwise} \end{array}$

Rotational stiffness (EC3)

Moment [kNm] — $\dfrac{M_{j.Ed}}{1000}$

Rotation [rad] — $\phi\left(M_{j.Ed}\right)$
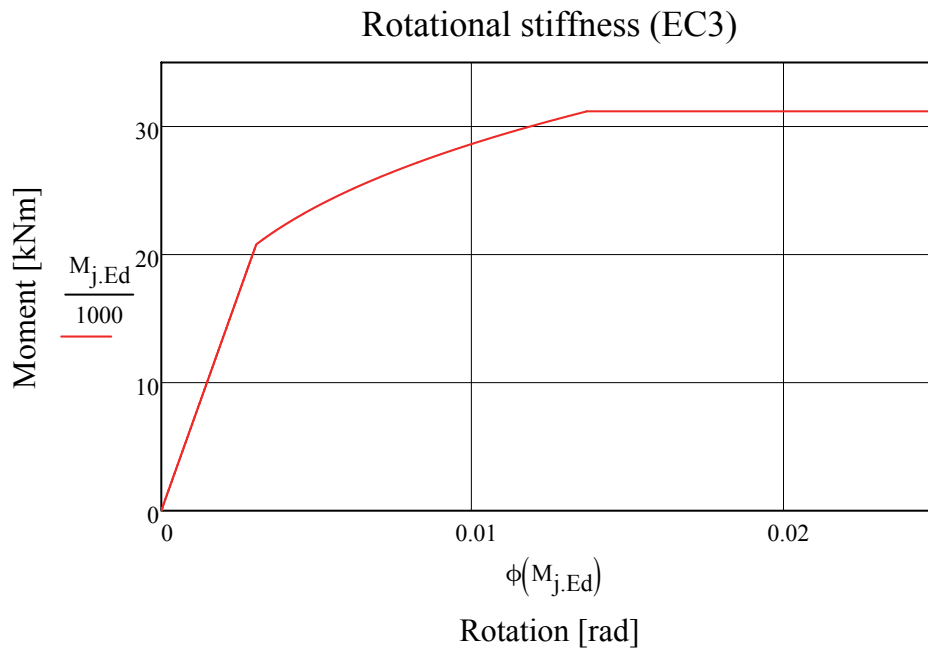
3. ROTATION CAPACITY

A joint can be modeled as a plastic hinge in the global analysis when the rotation capacity is sufficient. For a bolted joint with end-plate, both of the following conditions must be satisfied:

6.4.2.(2) a)
- The moment capacity of the joint is governed by resistance in column flange or end-plate.

The moment capacity is limited by failure of end-plate in bending => OK

6.4.2.(2) b)
- The thickness, t, of column flange or end-plate is limited by:

$$t \leq 0.36 \cdot d \cdot \sqrt{\frac{f_{ub}}{f_y}} = 9 \cdot mm$$

Minimum plate thickness:

$$t' := \min\left(t_{f.c}, t_p\right) = 12 \cdot mm \qquad \text{(end-plate)}$$

$$\text{Requirement} := \begin{vmatrix} \text{"OK"} & \text{if } t \leq 0.36 \cdot d \cdot \sqrt{\frac{f_{ub}}{f_y}} & = \text{"NOT OK"} \\ \text{"NOT OK"} & \text{otherwise} \end{vmatrix}$$

The joint do <u>not</u> satisfy the requirements for rigid plastic global analysis. => Either increasing bolt diameter (M24) or reduce end-plate thickness (8 mm).
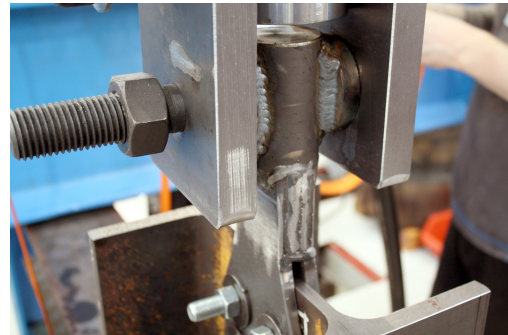
C   Additional pictures of the experimental tests

Portal frame structure and the 1000 kN hydraulic actuator
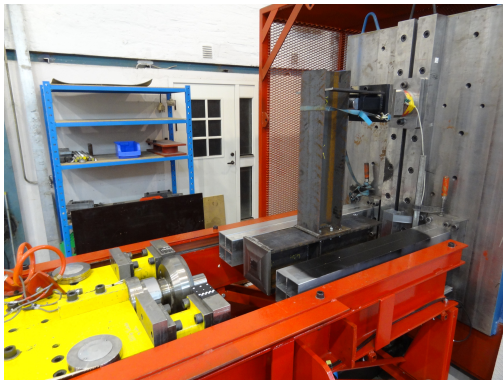

Steel angle with circular support.
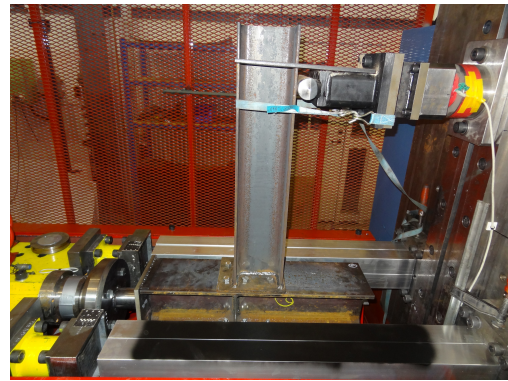

Fin plate component bolted to the column web.

Figure C.56: *Pictures of quasi-static test setup.*

Kicking machine used to accelerate the trolley.

Trolley and the test specimen mounted to the reaction wall.

Side view showing the extended support structure.

Figure C.57: *Pictures of dynamic test setup.*